JOURNAL OF GEOPHYSICAL RESEARCH, VOL. 98, NO. B5, PAGES 8225–8241, MAY 10, 1993

Travel Times of *S* and *SKS*: Implications for Three-Dimensional Lower Mantle Structure Beneath the Central Pacific

E. J. GARNERO AND D. V. HELMBERGER

Seismological Laboratory, California Institute of Technology, Pasadena

The travel times of *S* and *SKS* phases from deep-focus Fiji-Tonga events recorded in North America by Canadian Station Network and World Wide Seismographic Station Network stations exhibit a strong azimuthal dependence. The differential times of *S-SKS* exhibit relatively little scatter and are used to investigate three-dimensional mantle models for the central Pacific region. *S-SKS* times are corrected for Earth's ellipticity, and residuals are computed with respect to the iasp91 reference model. Anomalously large *S-SKS* times, ranging up to 9 s larger than iasp91 predictions for $\Delta > 100°$, suggest a slow lower mantle beneath the central Pacific. These results are compared to the predictions of three tomographic models: MDLSH of Tanimoto (1990), model SH12_WM13 of Su et al. (1992), and model SH.10c.17 of Masters et al. (1992). The three-dimensional whole mantle models have been parameterized into 11 spherical shells. Qualitative agreement between the tomographic model predictions and observations is encouraging, varying from fair to good. However, inconsistencies are present and suggest anomalies in the lower mantle of scale length smaller than the present 2000+ km scale resolution of tomographic models. Laterally varying outer core structure is not necessary to explain the anomalies in this data set, although such a scenario cannot be resolved with this data.

INTRODUCTION

In the past few years, the lowermost mantle beneath the Pacific ocean has been characterized as having anomalously slow seismic velocities with a circum-Pacific fringe of high velocities. This large-scale structure has been inferred by seismic tomography using body waves [e.g., *Dziewonski and Woodhouse*, 1987], surface waves [e.g., *Tanimoto*, 1990], as well as normal modes [e.g., *Li et al.*, 1991]. This slow V_S region has been observed by nontomographic body wave studies as well. For example, using *ScS-S* differential travel times, *Woodward and Masters* [1991] identify a very slow lower mantle region beneath the southwest Pacific, with residuals up to 8 s. This same anomaly was noted previously by *Sipkin and Jordan* [1980] using multiple *ScS* travel times. This region corresponds to the southwest part of the slow central Pacific anomaly seen in the tomographic models. Also, *Garnero et al.* [1988] analyzed differential travel times of *SnKS* waves to infer a laterally varying slow lower mantle beneath the central Pacific, with *S-SKS* times up to 8 s larger than predictions. Any seismic information on this region has particular relevance to models of mantle dynamics and geochemistry, as well as models of heat flow from the core. Such issues relate directly to the nature of mantle convection and plume formation. Whether the central Pacific lower mantle is the site of mantle upwelling may eventually be addressed by the seismic tomography models, but information concerning the details of such features exists primarily in the smaller wavelengths. Tomographic models of the lower mantle beneath the central Pacific often correlate at longer periods, while differing the most at smaller wavelengths. The purpose of this paper is to compare direct travel time measurements with predictions of the three-dimensional (3-D) mantle models as a first step towards understanding the 3-D lower mantle *S* wave anomalies beneath the Pacific.

Paper number 93JB00147.
0148-0227/93/93JB-00147$05.00

S-SKS differential travel times are ideal for comparison to time predictions of 3-D mantle models to assess lower mantle *S* wave velocity structure (V_S) beneath the central Pacific. Differential times have the advantage over absolute times in that source and receiver complexities are suppressed. For the lower mantle beneath the central Pacific, deep-focus Fiji-Tonga earthquakes recorded in North and South America are well suited for such an investigation. The dense station arrays of the World-Wide Seismographic Station Network (WWSSN) and the Canadian Seismic Network (CSN) make possible a detailed sampling of the mid-Pacific lower mantle region.

DATA SET

Long- and short-period seismograms have been used from 13 Fiji-Tonga earthquakes recorded in North and South America by WWSSN and CSN stations. The hypocentral information as reported by the International Seismological Centre (ISC) is given in Table 1. All events used were deep focus except one midfocus event (event 3, Table 1). The path coverage from the Fiji-Tonga events recorded on the North and South American stations is shown in Figure 1. The great circle paths show the dense ray coverage where the *S* wave passes through the bottom of the mantle beneath the central and eastern Pacific.

A sample profile of long-period recordings of *SKS* and *S* is shown in Figure 2. The longitudinal *SV* components shown have been obtained by rotating the digitized horizontal records into their great circle longitudinal and transverse components. In Figure 2*a*, the *SV* traces have been plotted with absolute time, along with predictions of the reference Earth model iasp91 of *Kennett and Engdahl* [1991] as dashed lines. The travel time delays for *SKS* and *S* with respect to iasp91 are indicated by the numbers in Figure 2*a*. For example, at station DUG (Dugway, Utah), *SKS* and *S* are late by 6.6 and 8.0 s, respectively. Large delays for this station have been noted in previous studies [e.g., *Graves and Helmberger*, 1988]. However, shifting the *SKS* arrivals to line up with the iasp91 prediction for *SKS*, as seen in Figure

TABLE 1. Hypocentral Information of Fiji-Tonga Events

Event	Date	Origin Time, UT	Latitude	Longitude	Depth, km	M_b
1	Dec. 28, 1964	1616:08.7	−22.13	−176.62	577	5.2
2	March 17, 1966	1550:32.3	−21.08	−179.15	627	5.9
3	Aug. 12, 1967	0939:45.7	−24.79	−177.38	144	6.0
4	Oct. 9, 1967	1721:46.2	−21.10	−179.18	605	6.2
5	Jan. 24, 1969	0233:03.4	−21.87	−179.54	587	5.9
6	June 28, 1970	1109:51.3	−21.66	−179.42	587	5.8
7	Nov. 20, 1971	0727:59.5	−23.45	−179.88	533	6.0
8	March 30, 1972	0534:50.4	−25.69	179.58	479	6.1
9	Dec. 28, 1973	0531:03.8	−23.88	−179.99	517	6.2
10	March 23, 1974	1428:33.0	−23.93	179.88	504	6.0
11	Oct. 21, 1974	0412:28.7	−17.97	−178.49	596	5.9
12	July 20, 1980	2120:03.6	−17.88	−178.61	588	6.0
13	April 28, 1981	2114:47.1	−23.70	−179.99	522	6.0

2*b*, illustrates the stability in the differential travel time of *S* and *SKS* ($T_{S\text{-}SKS}$) in the data. The *S-SKS* anomalies with respect to iasp91 are indicated by the numbers and show that $T_{S\text{-}SKS}$ in the data is up to around 7 s larger than that predicted by iasp91 for this profile. The large anomalies in Figure 2*a* may be due to upper mantle structure. The *S-SKS* differential time anomalies in Figure 2*b*, however, are more related to the deep Earth where *SKS* and *S* travel very different paths. They will be explored in further detail in a later section. A mislocation in source depth by 50 km will only produce a 0.7 s change in $T_{S\text{-}SKS}$. In these profiles, all amplitudes have been normalized to the maximum amplitude of the trace.

TRAVEL TIME OBSERVATIONS

The times of *S* and *SKS* (T_S and T_{SKS}, respectively) were measured by picking the onset time of the phase using synthetic seismograms as a guide (as from *Grand and Helmberger* [1985]). This measurement was only made in cases where the phase of interest was well above the noise level. For digitized data, these picks were made on a computer graphics screen using a mouse and cross-hairs. T_S was measured on the *SV* component for the digitized data.

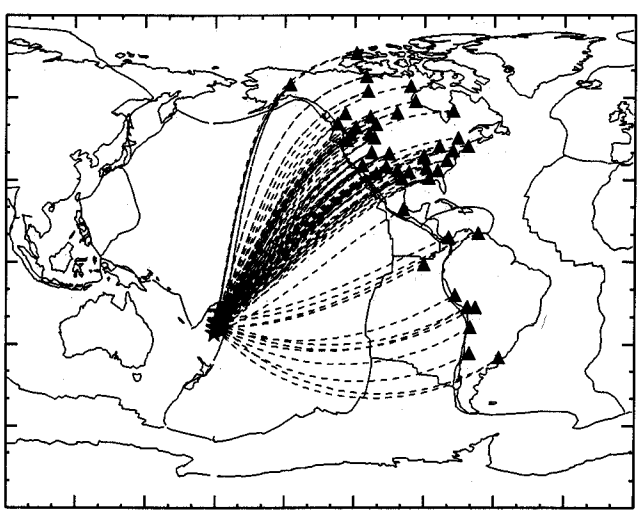

Fig. 1. Map of the world showing great circle ray paths from Fiji-Tonga events (stars) to North and South American stations (triangles).

For this data set, no discrepancy could be seen between $T_S(SH)$ and $T_S(SV)$. For records that were not digitized, measurements were made on the paper records on the north-south and east-west components and cross checked for accuracy. If the short-period recordings had good signal to noise ratio, they were also measured as a check of the long-period times. For a given event-station pair, if any measurements from the different components of the nonrotated paper records gave discrepant times by up to 0.3 s, they were discarded from the data set. Of all the data gathered for the 13 events in Table 1, 110 measurements of each of T_S and T_{SKS} were kept. These times were then differenced to obtain the $T_{S\text{-}SKS}$ differential time. This greatly increases the size of our previous *S-SKS* data set of 33 measurements for the same region [*Garnero et al.*, 1988].

The observed T_S, T_{SKS}, and those corrected for Earth's ellipticity [*Dziewonski and Gilbert*, 1976], T_S^{ell} and T_{SKS}^{ell}, respectively, are presented in Table 2. The ellipticity corrected times are used to calculate the $T_{S\text{-}SKS}$ times in Table 2 and presented with those predicted by the iasp91 model (for the appropriate depths and distances). Also listed are the differences between the observed and predicted times of *S*, *SKS*, and *S-SKS* (δT_S, ΔT_{SKS}, and $\delta T_{S\text{-}SKS}$, respectively). We define these residual times as the observed minus predicted:

$$\delta T_S = (T_S)_{\text{obs}} - (T_S)_{\text{iasp91}}$$

$$\delta T_{SKS} = (T_{SKS})_{\text{obs}} - (T_{SKS})_{\text{iasp91}}$$

$$\delta T_{S\text{-}SKS} = (T_{S\text{-}SKS})_{\text{obs}} - (T_{S\text{-}SKS})_{\text{iasp91}}.$$

All travel time anomalies were rounded off to the nearest tenth of a second. These residual travel times are plotted in Figure 3 as a function of distance. No station corrections have been applied. Figure 3*a* shows that δT_S times are anomalously large, by as much as 10 s in many cases, and at first glance appear very scattered. δT_{SKS} times are less scattered than δT_S and between 82° and 95° show a slight trend of decreasing with distance. $\delta T_{S\text{-}SKS}$ times are given in Figure 3*c*. Differencing the *S* and *SKS* times helps to suppress some of the scatter seen in Figures 3*a* and 3*b* and reveals an apparent trend with $\delta T_{S\text{-}SKS}$ increasing with distance. This suggests that much of the scatter in the absolute travel times of Figure 3*a* is due to near source or near receiver regions. Variations in upper mantle shear

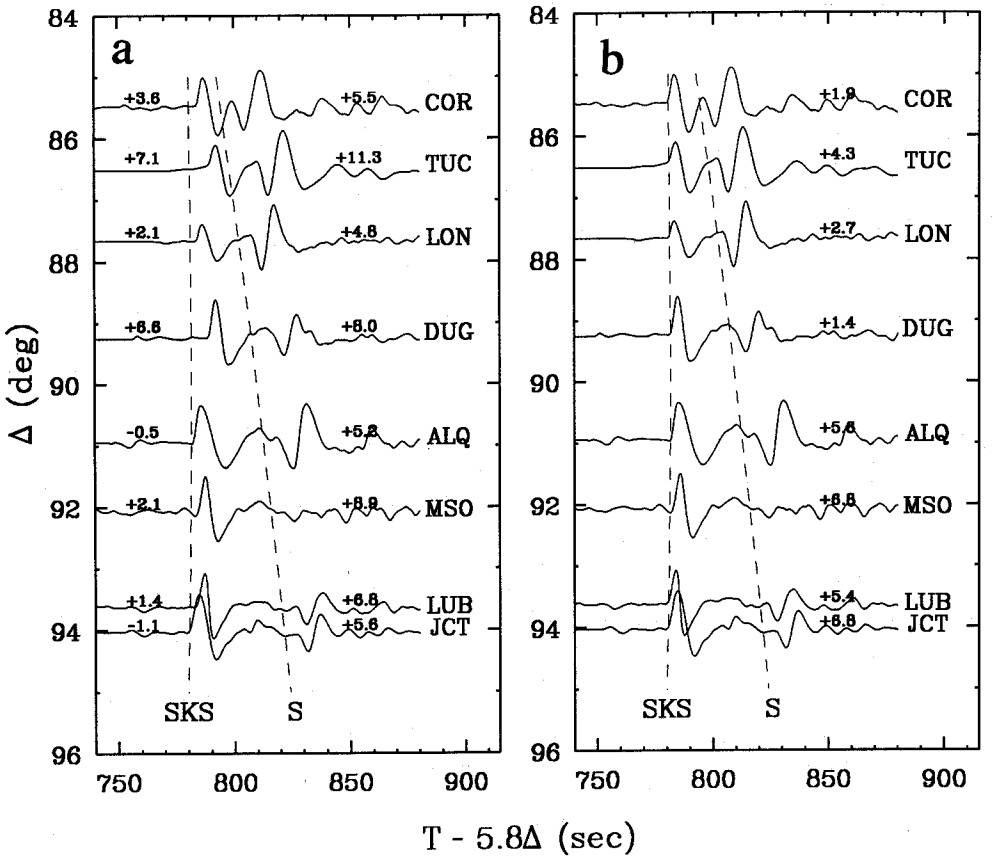

Fig. 2. Sample data from event 13 in Table 1. Radial components are shown for *SKS* and *S* along with predictions of iaspi as dashed lines. (*a*) Traces plotted absolutely in time. Numbers are *SKS* and *S* anomalies with respect to iasp91; (*b*) *SKS* phase is lined up with iasp91 prediction. Numbers are *S-SKS* anomalies with respect to iasp91.

structure under North America is expected to cause at least 5 to 6 s variations [*Lay and Helmberger*, 1983; *Grand*, 1987]. The same residual travel times are plotted as a function of azimuth in Figure 4. In Figures 4*a*, 4*b*, and 4*c*, a tendency for residuals to increase between the azimuths of 10° and 65° (from NNE to ENE from Fiji-Tonga) is apparent. With pronounced distance and azimuthal trends in the observations, a closer look at the *S* and *SKS* times is necessary.

In Figure 5, the densely sampled azimuth range from 10° to 65° is divided up into three "pie slices." The boundaries of these slices are great circle paths. Data with paths to Central and South America are not included in the rest of the analysis due to their sparser core-mantle boundary (CMB) sampling for our data set (see Figure 1). Figure 6 displays the residual times with respect to distance, where the symbols are shaded to correspond to the azimuth slices of Figure 5. The open circles correspond to the most northerly azimuth slice from Fiji-Tonga to North America; the gray circles are for the intermediate azimuth slice; and the solid circles are measurements from the most easterly azimuth slice. In Figure 6*a*, the δT_S times are seen to systematically increase with increasing azimuth. The solid circles are systematically the most anomalously large δT_S, and the open circles are systematically the smallest δT_S, while the gray circles are intermediate between the open and solid circles, with some overlap of the solid circles. This trend indicates that increasingly slow velocities are encountered by the paths as the azimuth from the source region is increased clockwise from the north. This pattern also varies with azimuth from the strike of the slab, though slab effects on the *S* and *SKS* times for paths to the North American stations from the Tonga trench are expected to be minimal. *S* and *SKS* spend very little time in the slab, since the slab dips toward the west, striking around N15°E, and ray paths depart NNE from the underside of the slab. The azimuth range (relative to slab strike) of stations used here is such that slab effects are predicted to be absent (or small) [*Cormier*, 1989].

The δT_{SKS} times are displayed in Figure 6*b*. For distances greater than 95°, the data are scattered with a mean near 1 s. From about 83° to 90°, however, the mean of the measurements is greater than this with a slight negative trend. This may be due to 3-D lower mantle structure in the central Pacific or outermost core structure and will be addressed in the following section. Figure 6*c* shows the residual times $\delta T_{S\text{-}SKS}$. The trends for the different azimuth slices are clearly present, with the easterly azimuth (solid circles) measurements on average the most anomalous. The scatter for this 50°–65° azimuth slice is reduced for $\delta T_{S\text{-}SKS}$ in comparison to that of δT_S or δT_{SKS} in Figures 6*a* and 6*b*. The scatter for the 25°–50° slice is also reduced. For each azimuth bin, the residuals increase at larger delta in Figure 6*c*. To further illustrate that the $\delta T_{S\text{-}SKS}$ times from the three different azimuth sectors behave differently, Figure 7 shows a simple least squares fit of a line to the data from different azimuth slices. It is possible that the error in such a fit may be decreased by fitting a polynomial to the data,

TABLE 2. All *S* and *SKS* Travel Times With Respect to Events and Hypocentral Information in Table 1

Station Information			Observed					iasp91			Observed-iasp91		
Station	Δ	Azimuth, deg	T_S	T_{SKS}	T_S^{ell}	T_{SKS}^{ell}	T_{S-SKS}	T_S	T_{SKS}	T_{S-SKS}	δT_S	δT_{SKS}	δT_{S-SKS}
						Event 1							
TUC	85.17	52.5	1287.5	1271.5	1287.1	1271.2	16.0	1278.5	1265.0	13.5	8.6	6.2	2.5
ALQ	89.59	52.0	1326.2	1293.1	1325.9	1292.9	33.1	1319.2	1291.5	27.7	6.7	1.4	5.4
COL	90.16	13.0	1320.5	1291.2	1321.6	1292.4	29.2	1324.3	1294.8	29.5	−2.7	−2.3	−0.3
BOZ	91.30	40.7	1339.7	1303.8	1339.9	1304.1	35.8	1334.3	1301.2	33.1	5.6	2.9	2.7
GOL	92.53	48.1	1350.6	1314.0	1350.5	1314.0	36.5	1345.0	1308.0	37.0	5.5	6.0	−0.5
						Event 2							
COR	82.85	36.7	1253.5	1246.3	1253.7	1246.6	7.1	1248.3	1241.7	6.6	5.4	4.9	0.5
TUC	84.19	52.4	1269.3	1254.8	1268.9	1254.5	14.5	1261.3	1250.3	11.0	7.6	4.2	3.5
LON	85.01	35.6	1271.7	1256.8	1272.0	1257.2	14.8	1269.1	1255.4	13.7	2.9	1.8	1.1
DUG	86.72	44.7	1290.0	1271.3	1290.0	1271.3	18.6	1285.2	1265.9	19.3	4.8	5.4	−0.7
ALQ	88.60	51.8	1312.0	1280.2	1311.7	1280.0	31.8	1302.4	1277.1	25.3	9.3	2.9	6.5
COL	89.04	12.9	1303.0	1277.3	1304.1	1278.5	25.6	1306.3	1279.6	26.7	−2.2	−1.1	−1.1
JCT	90.23	40.5	1322.5	1290.0	1322.7	1290.3	32.4	1316.9	1286.5	30.4	5.8	3.8	2.0
LUB	91.44	54.7	1333.9	1295.3	1333.5	1295.0	38.6	1327.4	1293.3	34.2	6.1	1.7	4.4
GOL	91.50	47.9	1333.8	1298.0	1333.7	1298.0	35.7	1328.0	1293.6	34.4	5.7	4.4	1.3
JCT	91.80	58.2	1338.1	1298.7	1337.6	1298.2	39.4	1330.6	1295.3	35.3	7.0	2.9	4.1
						Event 3							
LON	87.10	34.7	1381.4	1364.6	1381.7	1365.0	16.7	1376.7	1362.2	14.4	5.0	2.8	2.3
PHC	87.12	29.2	1380.2	1363.4	1380.7	1364.0	16.7	1376.9	1362.4	14.5	3.8	1.6	2.2
UNM	87.81	67.8	1389.7	1369.3	1388.8	1368.5	20.4	1383.4	1366.6	16.8	5.4	1.9	3.6
ALQ	89.64	51.0	1407.8	1379.5	1407.6	1379.3	28.3	1400.4	1377.5	22.9	7.2	1.8	5.4
BOZ	92.00	39.9	1426.4	1394.4	1426.7	1394.7	31.9	1421.7	1391.1	30.6	5.0	3.6	1.3
SES	95.01	36.2	1451.5	1409.2	1452.0	1409.7	42.2	1447.9	1407.6	40.3	4.1	2.1	1.9
EDM	95.38	33.0	1454.3	1410.1	1454.9	1410.8	44.1	1451.1	1409.6	41.5	3.8	1.2	2.6
MBC	106.84	12.3	1550.1	1465.7	1551.5	1467.2	84.3	1547.0	1464.8	82.3	4.5	2.4	2.0
						Event 4							
PHC	84.74	30.2	1271.0	1256.3	1271.5	1256.9	14.6	1270.0	1257.5	12.5	1.5	−0.6	2.1
COL	89.07	12.9	1305.5	1279.2	1306.6	1280.3	26.2	1310.1	1283.6	26.5	−3.5	−3.3	−0.3
BOZ	90.26	40.5	1324.5	1290.4	1324.7	1290.7	34.0	1320.6	1290.4	30.2	4.1	0.3	3.8
SES	93.03	36.6	1346.3	1303.5	1346.7	1304.0	42.7	1344.8	1305.8	38.9	1.9	−1.8	3.8
EDM	93.21	33.4	1347.3	1303.9	1347.8	1304.5	43.3	1346.3	1306.8	39.5	1.5	−2.3	3.8
YKC	97.56	25.1	1383.3	1326.6	1384.2	1327.6	56.6	1383.1	1329.4	53.6	1.1	−1.8	3.0
FFC	99.87	35.1	1404.1	1339.2	1404.7	1339.8	64.9	1402.3	1340.8	61.5	2.4	−1.0	3.4
ARE	99.87	112.0	1411.5	1341.4	1410.3	1340.2	70.1	1402.3	1340.8	61.5	8.0	−0.6	8.6
CMC	100.16	20.4	1405.3	1338.6	1406.4	1339.8	66.6	1404.7	1342.2	62.5	1.7	−2.4	4.1
LPA	101.20	134.4	1417.8	1344.8	1417.2	1344.2	73.1	1413.4	1347.2	66.2	3.8	−3.0	6.9
SHA	101.32	61.6	1423.2	1347.7	1422.7	1347.2	75.5	1414.4	1347.7	66.7	8.3	−0.5	8.8
BHP	102.10	85.2	1427.7	1348.6	1426.5	1347.4	79.1	1420.9	1351.4	69.5	5.6	−4.0	9.6
						Event 5							
COR	83.70	36.8	1268.6	1257.6	1268.8	1257.9	10.9	1262.8	1254.0	8.8	6.0	3.9	2.1
TUC	84.95	52.5	1284.2	1266.6	1283.8	1266.3	17.6	1274.8	1261.9	12.9	9.0	4.4	4.7
LON	85.86	35.7	1286.2	1269.3	1286.5	1269.7	16.8	1283.4	1267.5	15.9	3.1	2.2	0.9
PNT	88.60	34.6	1311.6	1286.1	1312.0	1286.6	25.4	1308.7	1284.0	24.7	3.3	2.6	0.7
ALQ	89.37	51.9	1323.9	1290.1	1323.6	1289.9	33.8	1315.6	1288.5	27.2	8.0	1.4	6.6
FSJ	89.51	28.8	1315.9	1288.1	1316.5	1288.8	27.7	1316.9	1289.3	27.6	−0.4	−0.5	0.1
COL	89.89	13.0	1316.5	1291.0	1317.6	1292.2	25.4	1320.3	1291.4	28.8	−2.7	0.8	−3.4
LUB	92.19	54.8	1346.5	1306.1	1346.1	1305.8	40.4	1340.4	1304.4	36.0	5.7	1.4	4.4
SES	93.85	36.7	1359.4	1314.5	1359.8	1315.0	44.8	1354.7	1313.4	41.3	5.1	1.6	3.5
EDM	94.03	33.6	1358.4	1313.9	1359.0	1314.5	44.4	1356.3	1314.3	41.9	2.7	0.2	2.5
DAL	95.82	57.2	1378.7	1327.2	1378.3	1326.8	51.5	1371.5	1323.8	47.7	6.8	3.1	3.8
YKC	98.40	25.3	1396.3	1337.1	1397.3	1338.1	59.1	1393.0	1336.8	56.2	4.3	1.3	2.9
FFC	100.69	35.3	1415.4	1348.0	1416.0	1348.7	67.4	1412.1	1347.9	64.1	3.9	0.8	3.3
CMC	100.99	20.5	1414.6	1348.8	1415.7	1350.0	65.7	1414.6	1349.3	65.2	1.1	0.7	0.5
OXF	102.16	57.8	1432.2	1354.7	1431.8	1354.4	77.5	1424.3	1354.8	69.5	7.5	−0.4	8.0
LPB	102.77	113.9	1435.0	1354.7	1433.8	1353.5	80.3	1429.4	1357.7	71.7	4.4	−4.2	8.6
MBC	104.42	12.4	1442.2	1364.7	1443.6	1366.1	77.4	1443.1	1365.1	78.0	0.5	1.0	−0.6
FCC	106.13	32.8	1462.7	1371.6	1463.5	1372.4	91.1	1457.3	1372.7	84.7	6.2	−0.3	6.4
BLC	106.72	27.0	1468.8	1378.3	1469.8	1379.3	90.4	1462.3	1375.2	87.1	7.5	4.1	3.3
AAM	108.60	51.3	1481.4	1378.7	1481.4	1378.7	102.7	1477.9	1383.2	94.8	3.5	−4.5	7.9
BLA	109.91	57.1	1496.7	1388.9	1496.4	1388.7	107.8	1488.8	1388.5	100.3	7.6	0.2	7.5
SCP	112.56	53.8	1520.6	1401.0	1520.5	1400.9	119.5	1510.9	1399.1	111.8	9.6	1.8	7.7
GWC	114.35	38.1	1535.0	1405.9	1535.6	1406.5	129.0	1525.8	1405.9	119.8	9.8	0.6	9.2
OTT	114.79	49.1	1541.2	1408.5	1541.3	1408.6	132.6	1529.4	1407.6	121.9	11.9	1.0	10.7

TABLE 2. (continued)

Station Information			Observed					iasp91			Observed-iasp91		
Station	Δ	Azimuth, deg	T_S	T_{SKS}	T_S^{ell}	T_{SKS}^{ell}	T_{S-SKS}	T_S	T_{SKS}	T_{S-SKS}	δT_S	δT_{SKS}	δT_{S-SKS}
						Event 6							
TUC	84.74	52.5	1281.1	1264.0	1280.7	1263.7	17.1	1272.8	1260.6	12.2	7.9	3.1	4.9
ALQ	89.16	51.9	1322.6	1289.6	1322.3	1289.4	33.0	1313.8	1287.2	26.5	8.6	2.2	6.5
COL	89.66	13.0	1314.2	1288.0	1315.3	1289.2	26.1	1318.2	1290.1	28.1	−2.9	−0.9	−2.0
GOL	92.08	48.0	1345.8	1307.7	1345.7	1307.7	38.0	1339.4	1303.8	35.7	6.3	3.9	2.3
JCT	92.32	58.3	1346.6	1305.2	1346.1	1304.7	41.4	1341.5	1305.1	36.4	4.6	−0.4	5.0
SHA	101.79	61.8	1430.8	1355.4	1430.3	1354.9	75.4	1421.2	1353.1	68.1	9.1	1.8	7.3
FLO	102.53	53.3	1434.0	1355.0	1433.8	1354.9	79.0	1427.4	1356.6	70.8	6.4	−1.7	8.2
ATL	105.64	60.0	1460.0	1371.2	1459.6	1370.8	88.8	1453.3	1370.5	82.8	6.3	0.3	6.1
CAR	114.61	88.3	1537.5	1405.7	1536.3	1404.4	131.8	1527.9	1406.9	121.0	8.4	−2.5	10.8
						Event 7							
COR	85.15	36.8	1290.1	1274.8	1290.3	1275.1	15.2	1285.3	1272.6	12.8	5.0	2.5	2.4
						Event 8							
JCT	95.20	58.9	1392.9	1341.6	1392.5	1341.2	51.3	1384.4	1340.0	44.4	8.1	1.2	6.9
						Event 9							
COR	83.91	47.3	1283.8	1268.0	1298.6	1281.0	17.6	1291.9	1278.0	13.9	6.7	3.0	3.7
ALQ	85.56	36.9	1298.4	1280.7	1350.6	1312.4	38.1	1341.1	1309.9	31.2	9.5	2.5	6.9
						Event 10							
COR	85.66	36.9	1301.2	1285.7	1301.4	1286.0	15.4	1295.0	1280.9	14.0	6.4	5.1	1.4
TUC	86.63	52.6	1312.8	1290.9	1312.5	1290.6	21.9	1304.1	1286.9	17.2	8.4	3.7	4.7
ALQ	91.06	52.2	1352.6	1314.1	1352.4	1313.9	38.4	1344.3	1312.9	31.4	8.1	1.0	7.0
COL	92.01	13.2	1349.4	1316.1	1350.5	1317.3	33.2	1352.6	1318.2	34.4	−2.1	−0.9	−1.2
MSO	92.26	39.0	1358.6	1318.6	1358.9	1319.0	39.9	1354.8	1319.6	35.2	4.1	−0.6	4.7
JCT	94.06	58.7	1375.2	1329.5	1374.7	1329.1	45.7	1370.3	1329.4	41.0	4.4	−0.3	4.7
GOL	94.07	48.4	1376.4	1333.4	1376.4	1333.4	42.9	1370.4	1329.4	41.0	6.0	4.0	1.9
DAL	97.38	57.6	1405.6	1347.8	1405.2	1347.5	57.8	1398.4	1346.7	51.8	6.8	0.8	6.0
						Event 11							
COL	85.89	12.6	1280.1	1267.2	1281.1	1268.3	12.8	1282.3	1266.2	16.1	−1.2	2.2	−3.3
ALQ	86.19	51.6	1293.3	1273.1	1292.9	1272.8	20.2	1285.1	1268.0	17.1	7.8	4.8	3.1
GOL	88.96	47.7	1317.9	1291.7	1317.7	1291.6	26.2	1310.5	1284.5	26.0	7.2	7.1	0.2
JCT	89.63	57.9	1325.4	1291.8	1324.8	1291.2	33.6	1316.5	1288.4	28.1	8.3	2.8	5.5
						Event 12							
SHA	99.31	60.9	1414.7	1348.0	1414.1	1347.4	66.7	1400.4	1341.1	59.3	13.7	6.3	7.4
FVM	99.39	53.3	1407.3	1345.1	1407.0	1344.8	62.2	1401.1	1341.5	59.6	5.9	3.3	2.6
BLA	106.98	55.8	1475.4	1380.8	1475.0	1380.5	94.6	1464.3	1376.1	88.1	10.7	4.4	6.5
SCP	109.47	52.4	1494.2	1389.7	1494.0	1389.5	104.5	1485.0	1386.6	98.4	9.0	2.9	6.1
WES	114.50	51.2	1538.3	1411.7	1538.2	1411.6	126.6	1526.8	1406.3	120.5	11.3	5.3	6.1
						Event 13							
COR	85.42	36.9	1295.0	1279.5	1295.2	1279.8	15.4	1289.7	1276.2	13.5	5.5	3.6	1.9
TUC	86.41	52.6	1310.7	1289.7	1310.4	1289.4	21.0	1299.1	1282.3	16.7	11.3	7.1	4.3
LON	87.60	35.9	1314.6	1291.2	1314.9	1291.6	23.3	1310.2	1289.5	20.6	4.8	2.1	2.7
DUG	89.13	45.0	1332.1	1305.1	1332.1	1305.2	26.9	1324.1	1298.6	25.5	8.0	6.6	1.4
GIE	89.44	90.7	1338.7	1306.5	1337.5	1305.3	32.2	1326.9	1300.4	26.5	10.6	4.9	5.7
ALQ	90.84	52.1	1344.7	1308.1	1344.5	1307.9	36.5	1339.3	1308.4	30.9	5.2	−0.5	5.6
COL	91.76	13.2	1345.6	1313.0	1346.7	1314.2	32.5	1347.4	1313.6	33.8	−0.7	0.6	−1.3
MSO	92.02	39.0	1358.3	1316.7	1358.6	1317.1	41.5	1349.7	1315.0	34.7	8.9	2.1	6.8
PEL	92.12	127.7	1351.6	1316.4	1351.0	1315.8	35.3	1350.5	1315.6	35.0	0.5	0.2	0.3
LUB	93.60	55.1	1370.4	1325.3	1370.1	1325.0	45.1	1363.3	1323.6	39.7	6.8	1.4	5.4
GOL	93.84	48.3	1373.3	1328.9	1373.3	1328.9	44.3	1365.4	1324.9	40.5	7.9	4.0	3.8
JCT	93.85	58.6	1371.6	1324.3	1371.1	1323.9	47.3	1365.5	1325.0	40.5	5.6	−1.1	6.8
NNA	97.00	106.4	1401.6	1344.4	1400.4	1343.2	57.2	1392.2	1341.4	50.8	8.2	1.8	6.4
ANT	97.01	119.7	1394.2	1341.2	1393.3	1340.2	53.0	1392.3	1341.5	50.8	1.0	−1.3	2.2
ARE	99.60	112.8	1423.0	1358.4	1421.9	1357.2	64.6	1413.8	1354.4	59.5	8.1	2.8	5.1
LPA	99.93	135.1	1418.4	1355.6	1417.9	1355.0	62.9	1416.6	1356.0	60.6	1.3	−1.0	2.3
SHA	103.22	62.3	1453.7	1373.6	1453.2	1373.1	80.1	1444.0	1371.4	72.5	9.2	1.7	7.6
FVM	103.87	54.6	1456.9	1372.8	1456.8	1372.7	84.1	1449.4	1374.4	75.0	7.4	−1.7	9.1
SCP	113.99	54.5	1542.5	1416.2	1542.4	1416.2	126.2	1533.6	1416.4	117.2	8.8	−0.2	9.0
CAR	115.20	89.5	1547.9	1420.6	1546.7	1419.4	127.3	1543.7	1420.9	122.8	3.0	−1.5	4.6

though the purpose of Figure 7 is merely to show that the data on average behave distinctly differently for the different azimuth binnings of Figure 5.

Since the δT_S residual times in Figure 6*a* increase with distance at large delta, the trend whereby $\delta T_{S\text{-}SKS}$ increases with distance can be explained by a slow lower mantle beneath the central Pacific that preferentially slows down S relative to SKS. Such a slow anomaly may also explain the

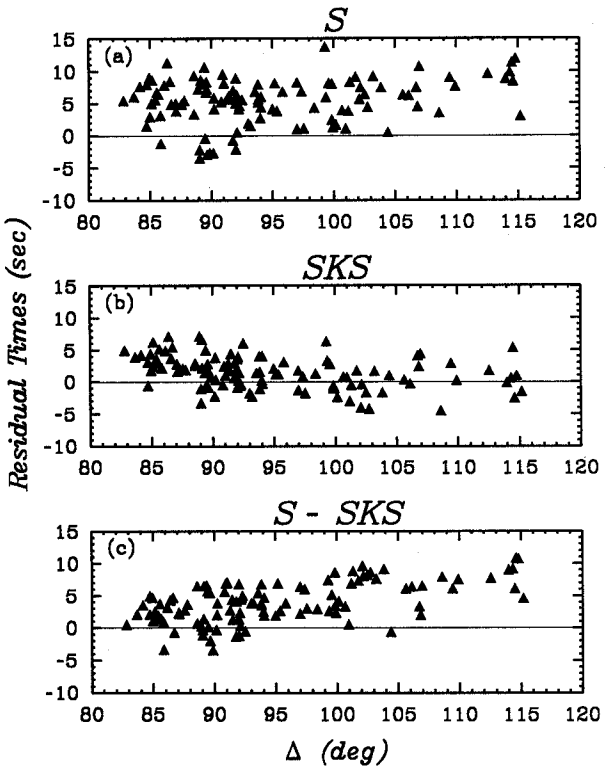

Fig. 3. Residual travel times (with respect to iasp91) of (*a*) *S*, (*b*) *SKS*, and (*c*) *S-SKS* are plotted as a function of distance for Fiji-Tonga events recorded in North and South America.

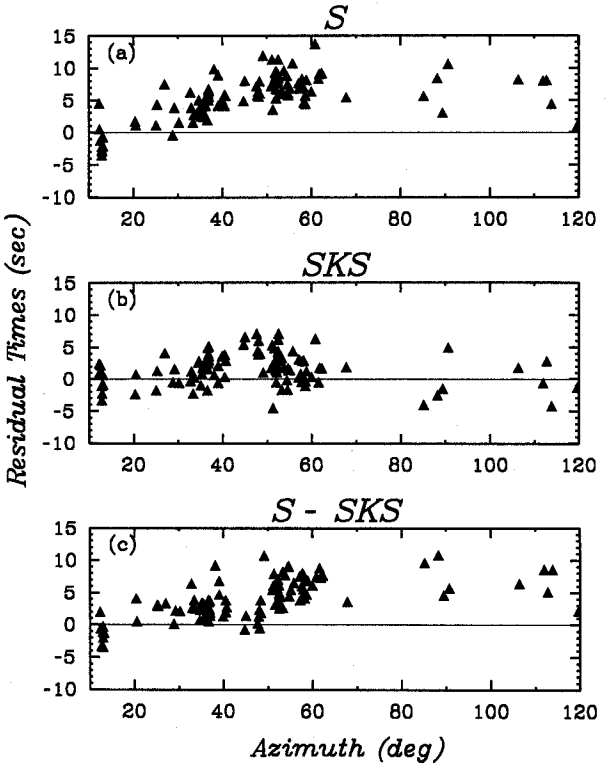

Fig. 4. Residual travel times (with respect to iasp91) of (*a*) *S*, (*b*) *SKS*, and (*c*) *S-SKS* are plotted as a function of azimuth from the Fiji-Tonga source region events recorded in North and South America.

anomalously slow δT_{SKS} seen in Figure 6*b* at $\Delta < 95°$, because *SKS* at smaller distances spends more time in the lower mantle than do larger distance *SKS* arrivals. Such two-dimensional (2-D) scenarios will be investigated more quantitatively in the following sections. First, we will address implications of different one-dimensional (1-D) models on the travel times of *SKS* and *S*.

One-Dimensional Model Implications

As reported by *Garnero et al.* [1988], 1-D lower mantle shear wave (V_S) structures fail to model the anomalously large central Pacific *S-SKS* observations. In principle, an approach can be taken whereby three different 1-D models are sought to individually explain observations form each azimuth window. However, any 1-D model having an anomalously slow lower mantle in effort to match the slow Fiji-Tonga *S* wave observations predicts *SKS* times that are much too slow for the whole distance range of observations. Such 1-D models also underpredict the $T_{S\text{-}SKS}$ anomaly, since both *S* and *SKS* are predicted slow; thus the predicted difference time is less anomalous than observed. While more emphasis is put on the differential times of *S* and *SKS*, the absolute times contain important information that can be used as constraints on different travel time experiments. However, since we do not make an effort to include source or receiver effects, only the general trends in the absolute times will be considered here.

SKS arrival times are highly sensitive to outer core velocity structure. In fact, *SnKS* (*SKS*, *SKKS*, etc.) times have been used in many studies to infer outer core velocity structure [e.g., *Randall*, 1970; *Hales and Roberts*, 1971; *Kind and Müller*, 1977; *Lay and Young*, 1990; *Souriau and Poupinet*, 1991; *Kohler and Tanimoto*, 1992]. In principle, the magnitude of the anomalous $\delta T_{S\text{-}SKS}$ times in Figure 6*c* can be modeled by using a much faster outer core model, such as that of *Randall* [1971], to speed up *SKS* relative to

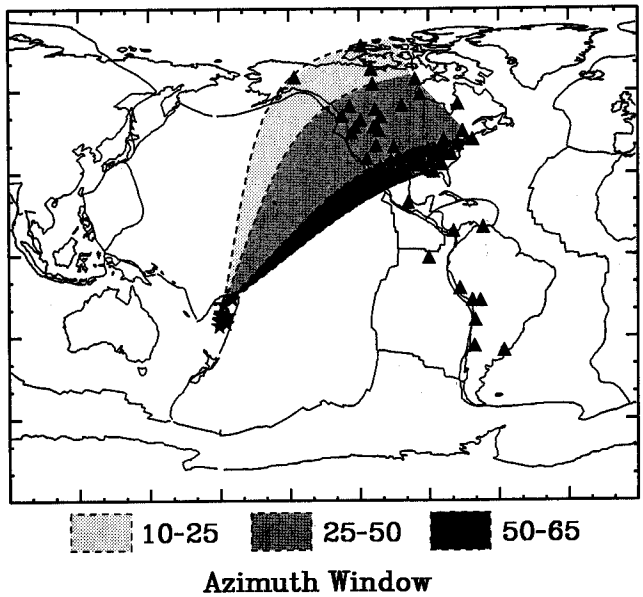

Fig. 5. Map of the world showing azimuth binning from Fiji-Tonga events (stars) to North American stations (triangles). The divisions between the shaded regions (dashed lines) are great circle paths.

S, thus increasing $T_{S\text{-}SKS}$, along with a slow lower mantle model to delay S times. Our S-SKS observations indicate that such a model would have to vary laterally over extended depth ranges in the outer core in order to model the data. Such large outer core P wave velocities (V_P) variations are routinely assumed highly unlikely due to the low viscosity in the outer core. Bounds on lateral velocity changes in the outer core are expected to be orders of magnitude smaller [*Stevenson*, 1987] than necessary to explain the S-SKS anomalies. Nevertheless, an attempt can be made to account for mantle side heterogeneity. In the recent study of *Kohler and Tanimoto* [1992], the 3-D mantle model of *Tanimoto* [1990] is subtracted out of long-period (33–100 s) $SnKS$ data to infer a ±5% variation in V_P in the outermost 200 km of the core. Such anomalies can produce ±5–6 s T_{SKS} anomalies for the extreme cases where SKS enters the outer core in a ±5% V_P anomaly, and exits the core through a 5% V_P anomaly of the same sign. For such a scenario to explain the $\delta T_{S\text{-}SKS}$ residuals plotted in Figure 6*c*, SKS times would have to be anomalously fast to produce a larger $T_{S\text{-}SKS}$ time, since SKS arrives before S for our distance range. Therefore attributing the anomalously large difference times of S and SKS to solely the outer core would require a faster outer core for our anomalous azimuths 25°–50° and 50°–65°. There is qualitative agreement between this requirement and the outer core V_P map of *Kohler and Tanimoto* [1992]. Unfortunately, the trade-off in outer core P velocity with lower mantle S velocity is an inherent feature of any $SnKS$ data set. In this study we choose to explore various 3-D lower mantle models, while keeping the outer core fixed as a laterally homogeneous model. This is motivated in part by the suggestion of Figure 6 that larger travel time anomalies exist for S and diffracted S than for SKS and also by our limitations of using only one phase of the $SnKS$ group, namely, SKS.

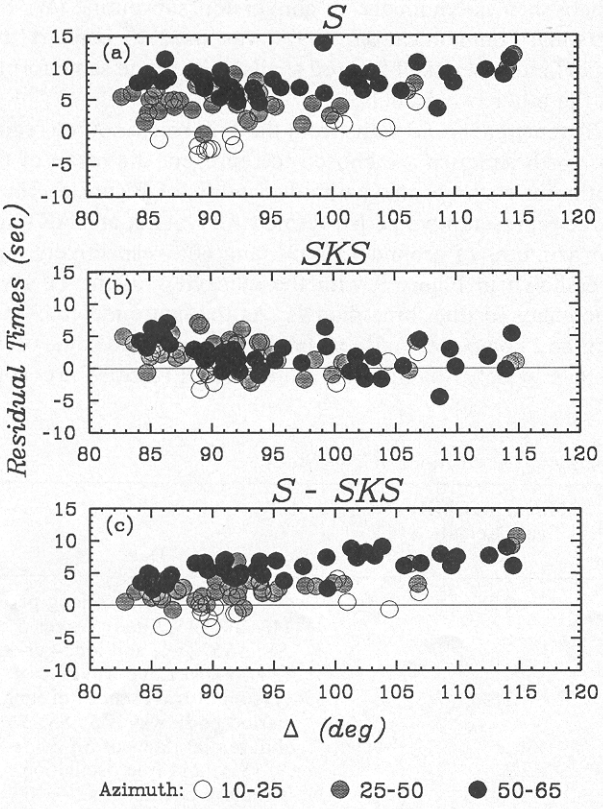

Fig. 6. Residual travel times (with respect to iasp91) of (*a*) S, (*b*) SKS, and (*c*) S-SKS are plotted as a function of distance for Fiji-Tonga events recorded in North America. The times are shaded to correspond to the azimuth slices of Figure 5.

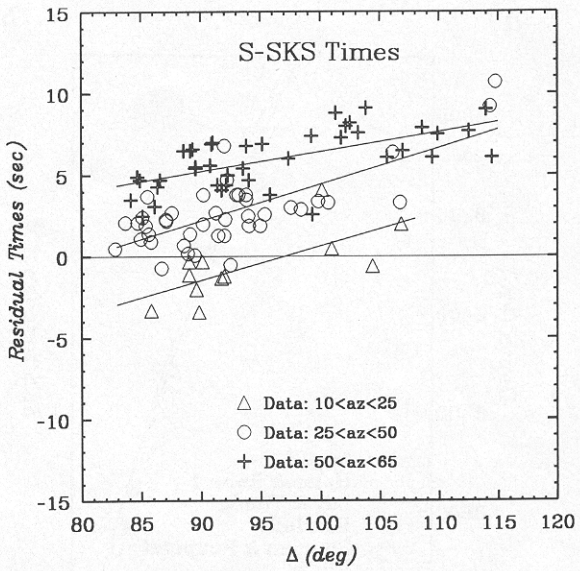

Fig. 7. Residual travel times (with respect to iasp91) of S-SKS are plotted as a function of distance with different symbols indicating the azimuth slice of Figure 5. The solid lines represent linear least square fits to the data for each of the three data groups.

The residual times of SKS in Figure 6*b* have a mean near 1 s in the distance range of $\Delta > 95°$, with scatter on the order of several seconds. To extract any deep Earth information from only SKS, source information and receiver structure must be assessed. However, differential travel times of $SnKS$ (e.g., $T_{SKKS\text{-}SKS}$, etc.) are useful for such modeling [*Schweitzer*, 1984; *Schweitzer and Müller*, 1986; *Lay and Young*, 1990; *Souriau and Poupinet*, 1991; *Kohler and Tanimoto*; 1992]. No effort is made here to resolve such differences, as we will concentrate mainly on the difference times of S and SKS. It is noted however that the δT_{SKS} times in Figure 6*b* are anomalously slow between 83° and 95°, tapering to near 1 s at larger distances. For this trend to be solely attributed to outer core V_P structure, an outer core model with a very slow outermost core would be necessary, along with an anomalously fast deeper core to produce the small mean in δT_{SKS} at larger distances ($\Delta > 95°$.) Figure 8*a* displays the outer core models of iasp91, *Hales and Roberts* [1971], *Lay and Young* [1990], *Randall* [1970], *Souriau and Poupinet* [1991], and *Dziewonski and Anderson* [1981]. The predictions of T_{SKS} residuals (with respect to iasp91) for these five outer core models are presented in Figure 8*b* along with the observations. The *Randall* [1970] model predicts the fastest SKS times, while the *Hales and Roberts* [1971] model predicts the slowest. The models of *Lay and Young* [1990], *Souriau and Poupinet* [1991], and *Dziewonski and Anderson* [1981] are intermediate between the latter two models and provide the best overall fit of the five models in Figure 8*a* to the data. However, effects of the mantle must be addressed before choosing an appropriate outer core model. For example, a very slow central Pacific D″ anomaly

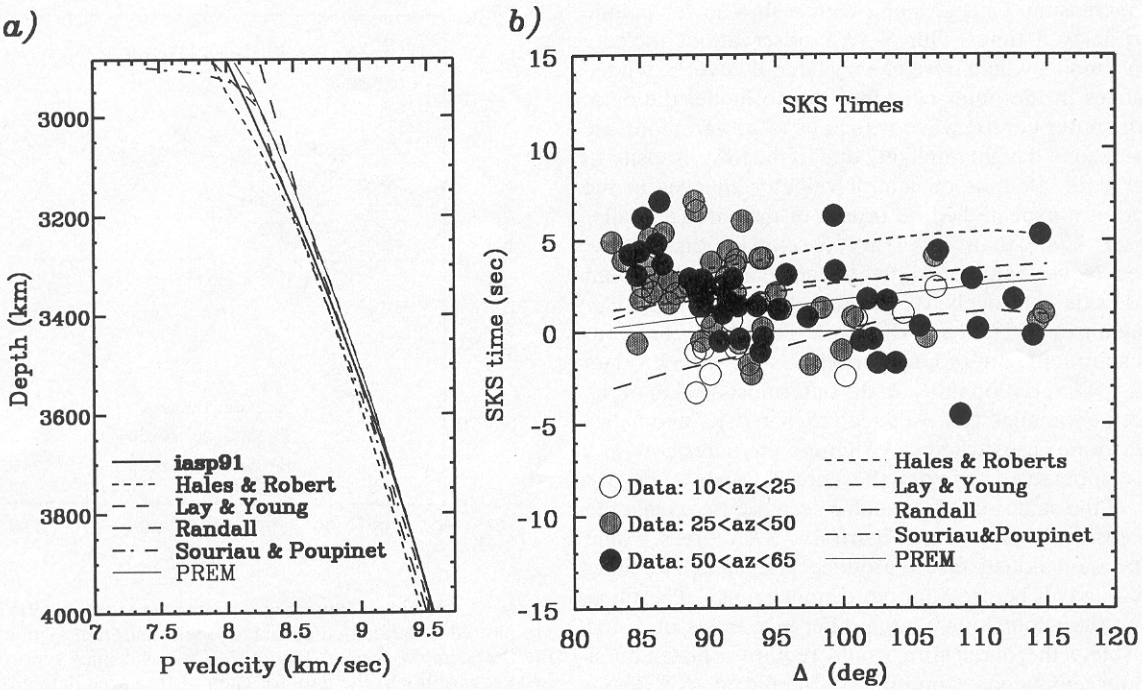

Fig. 8. (*a*) *P* wave velocity models of Earth's outer core. (*b*) Residual travel times (with respect to iasp91) of *SKS* observations (circles shaded to indicate azimuth) plotted with predictions of the outer core models of Figure 8*a*. The iasp91 mantle has been used for the calculations in Figure 8*b*.

will slow down *SKS* at the smaller distances, whose raypaths spend more time in the lower mantle than do large delta *SKS* paths. Such a scenario would be compatible with the δT_{SKS} observations at small delta (Figure 8*b*).

S-SKS Time Predictions From 3-D Models

In this section predictions for *S-SKS* times are made for three different 3-D tomographic V_S models of the mantle. The models used for comparison are MDLSH of *Tanimoto* [1990], SH.10c.17 of *Masters et al.* [1992], and SH12_WM13 of *Su et al.* [1992]. Basic information about these models is listed in Table 3. Models MDLSH and SH.10c.17 are parameterized with depth into 11 spherical shells for the whole mantle [see *Tanimoto*, 1990]. The thickness of the shells varies from around 180 km to 350 km thick. Model SH12_WM13, however, is parameterized vertically with Chebyshev polynomials. A conversion subroutine (W. Su, personal communication, 1992) was used to convert this model into a series of layered shells to be in the same format as the other two models.

Three great circle paths from the Fiji-Tonga source region to North America are chosen to represent the mean of the paths for each specific azimuth window of Figure 5. These three representative paths, termed AZ1, AZ2, and AZ3, are for azimuths of around 13°, 39°, and 60°, respectively, and are shown in Figure 9 with the map view of the D″ layer anomalies for the three models. As the figure indicates, the degree 2 component of the models is similar, but some of the details widely differ. Also shown in Figure 9 are solid

TABLE 3. Tomographic Models Used for T_{S-SKS} Predictions in This Study

Model	Researcher	Degree	Minimum CMB Scale Length, km	Data
MDLSH	*Tanimoto* [1990]	6	3400	waveform inversion of long-period (40–100 s) *SH* body waves *S*, *SS*, *SSS*, etc., and long-period (100–500 s) Love waves
SH.10c.17	*Masters et al.* [1992]	10	2100	inversion of travel times of long period body waves *S*, *SS*, *SSS*, differential times of *SS-S*, *ScS-S*, *sS-S*, and free oscillation structure coefficients
SH13_WM17	*Su et al.* [1992]	12	1800	joint inversion of travel times of *S*, *ScS* differential times of *SS-S*, *ScS-S*, and the waveforms of body and mantle waves

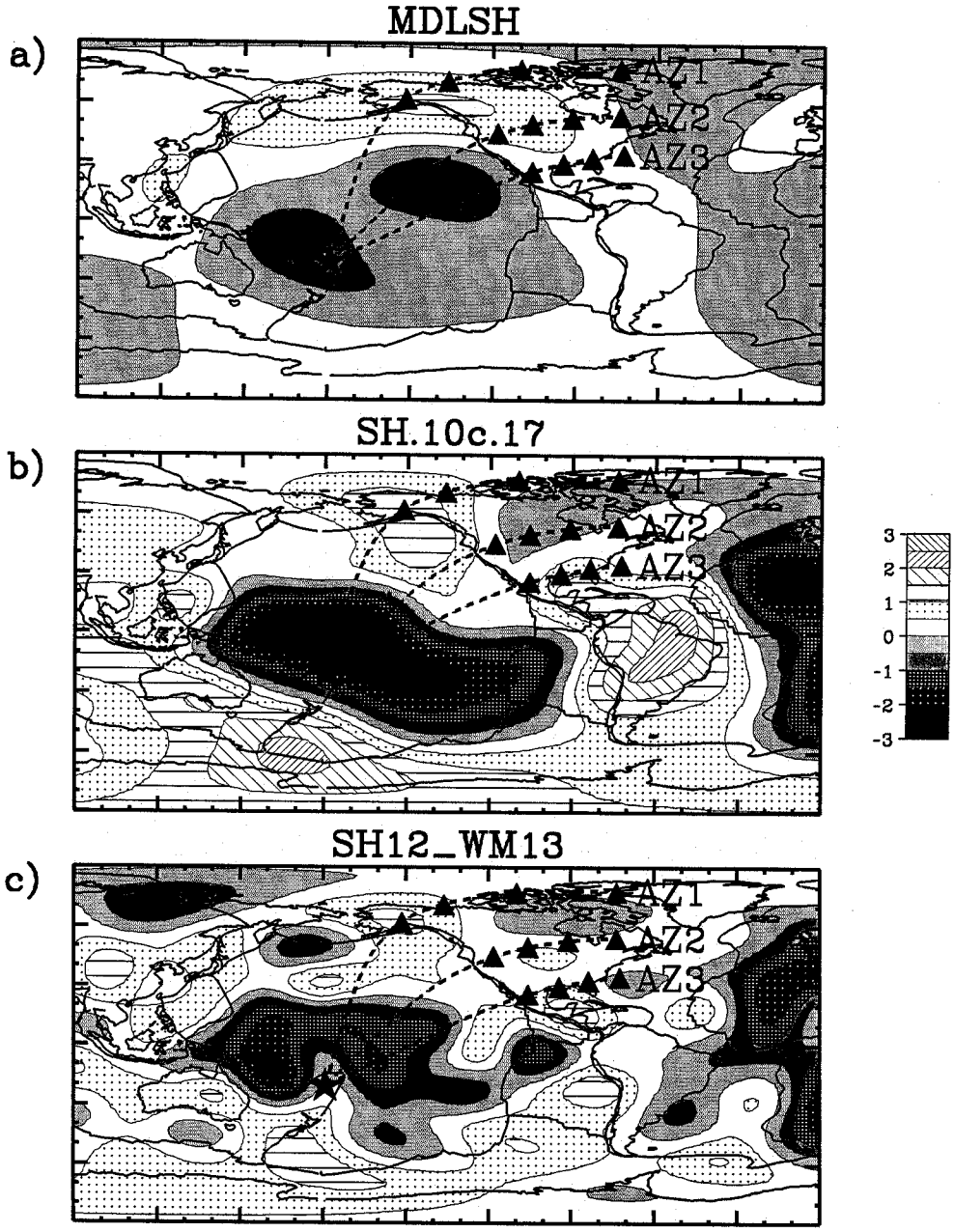

Fig. 9. Map views of the D″ layer of models (*a*) MDLSH, (*b*) SH.10c.17, and (*c*) SH12_WM13. Also shown for each are the three representative azimuths AZ1, AZ2, and AZ3 corresponding to the azimuth slices of Figure 5. The triangles indicate epicentral distances along the great circle paths of 85°, 95°, 105°, and 115°. Dark regions represent slower than average velocities, while light regions represent faster than average velocities.

triangles representing distances of 85°, 95°, 105°, and 115° along each path from a hypothetical Fiji-Tonga source at 500 km depth, latitude −20.0°, and longitude −179.0°. Here the assumption is made that the average of the $\delta T_{S\text{-}SKS}$ times for each azimuth window in Figure 6*c* can be modeled by a single great circle path 2-D cross section (one cross section for each azimuth window), based on the small scatter for each azimuth sector. $\delta T_{S\text{-}SKS}$ predictions of the tomographic models are made for these representative cross sections and the above hypothetical source and then compared to observations.

The technique employed to calculate $\delta T_{S\text{-}SKS}$ predictions for the tomography models assumes the ray paths of *S* and *SKS* from source to receiver are those of a laterally homogeneous Earth, and then the residuals for the specific paths and 3-D model are added up along each ray path. The predicted $\delta T_{S\text{-}SKS}$ residuals were obtained using the PREM reference model [*Dziewonski and Anderson*, 1981] since the residuals were originally derived with respect to PREM. Each of the 11 spherical shells where divided into a grid of blocks. Each block measures about 250 km square laterally, having the vertical dimension of the thickness of the spherical shell. V_S residuals for a specific model were then assigned to the 3-D network of blocks. This parameterization is convenient to calculate residuals for specific ray paths, though it is an approximation, see *Grand* [1987]. However,

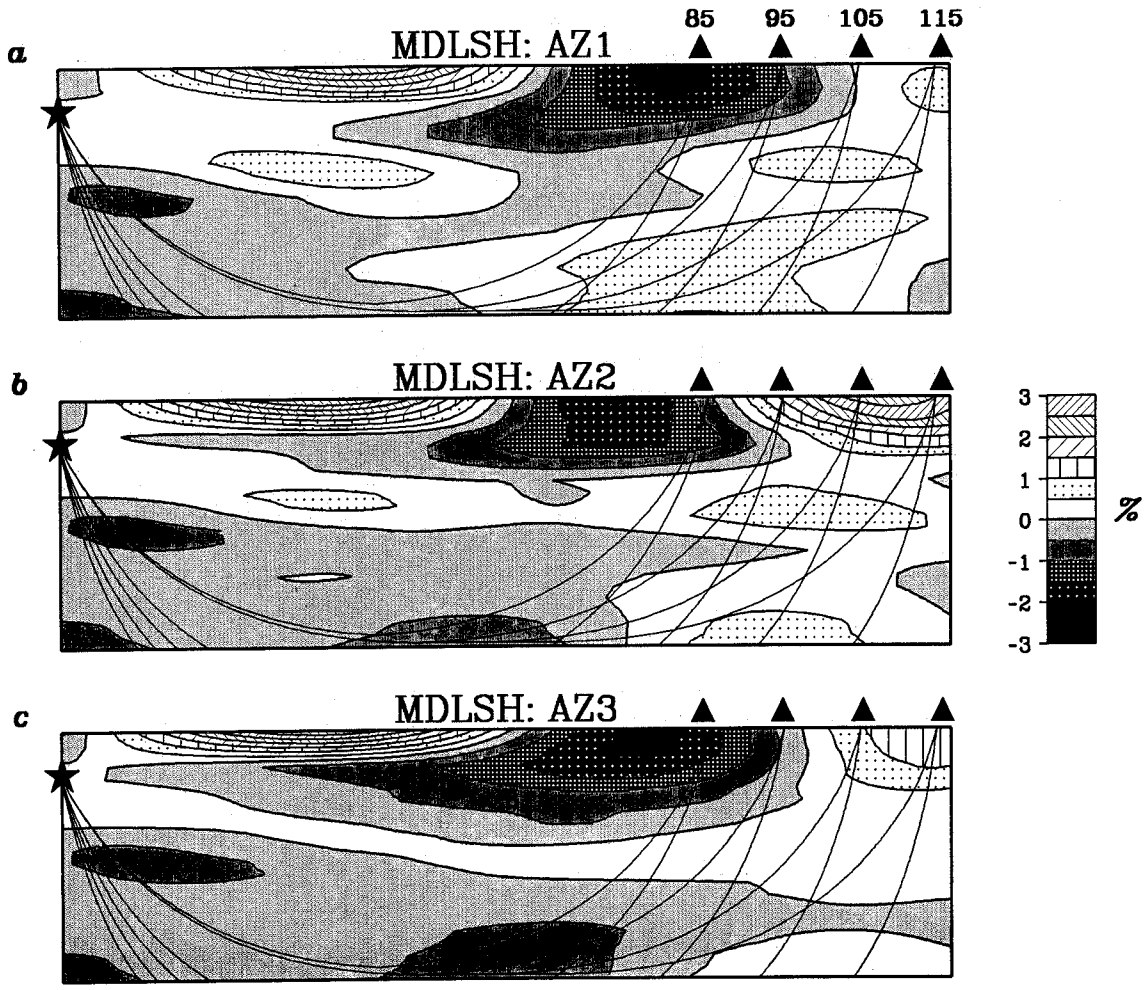

Fig. 10. Whole mantle cross sections from model MDLSH of *Tanimoto* [1990] for azimuths (*a*) AZ1, (*b*) AZ2, and (*c*) AZ3 of Figure 5. The vertical dimension of each plot is 2891 km, and the horizontal dimension is 115° in epicentral distance. V_S perturbations in percent are shown, where dark regions are slower than average, white and hatched regions are faster than average. The star and triangles for each cross section represent a 500-km-deep source at (−20, −179) and stations at 85°, 95°, 105°, and 115°, respectively. Also plotted are the mantle ray paths of *S* and *SKS* for the above distances.

with the horizontal length scales of features in the tomographic models being of the order of 3000 km and greater, such an approximation is justified.

For the following predictions of the residual times of *S* and *SKS*, the iasp91 core model has been used. Since we first wish to assess mantle affects on these travel times, the choice of a core model is arbitrary due to the trade-off mentioned above. The offset of any favored core model from the zero line of iasp91 in Figure 8*b* may be added to any of the 3-D predictions that follow. This will in affect adjust the $\delta T_{S\text{-}SKS}$ measurement to be that which includes the favored core model.

Model MDLSH Predictions

Whole mantle cross sections for the shear wave velocity model MDLSH of *Tanimoto* [1990] are presented in Figure 10 for the great circle paths in Figure 9 (Figures 10*a*, 10*b*, and 10*c* correspond to AZ1, AZ2, and AZ3, respectively). The contour plots are rectangular mappings of the mantle heterogeneities, where the vertical dimension of the box is the thickness of the mantle, and the horizontal dimension is 115° in arc. The actual horizontal dimension at Earth's surface (top of the box) is about 12800 km, while at the CMB (bottom of the box) it is ≈7000 km. Mapping of ray paths of *SKS* and *S* (and S_{diff}) for the laterally homogeneous model iasp91 [*Kennett and Engdahl*, 1991] are also shown for the distances 85°, 95°, 105°, and 115°. The V_S heterogeneities are plotted by percent, where dark regions indicate slower than average velocities, and white and hatched regions represent faster than average velocities. Model MDLSH predict a slow anomaly growing out of D″ beneath the central Pacific region in sweeping from AZ1 to AZ3. All of the *S* ray paths traverse this slow anomaly in the more easterly azimuths, but *SKS* paths miss it. This is in qualitative agreement with what might be needed to slow down *S* relative to *SKS* in order to model anomalously large *S*-*SKS* times. The actual $T_{S\text{-}SKS}$ residual time predictions of the cross-sections in Figure 10 are presented in Figure 11 (plotted with respect to iasp91) along with the data from Figure 6*c*. As in Figure 6*c*, the different symbols correspond to data from the three different azimuth slices of Figure 5. The lines represent the $\delta T_{S\text{-}SKS}$ time predictions of MDLSH. The line with long dashes is for

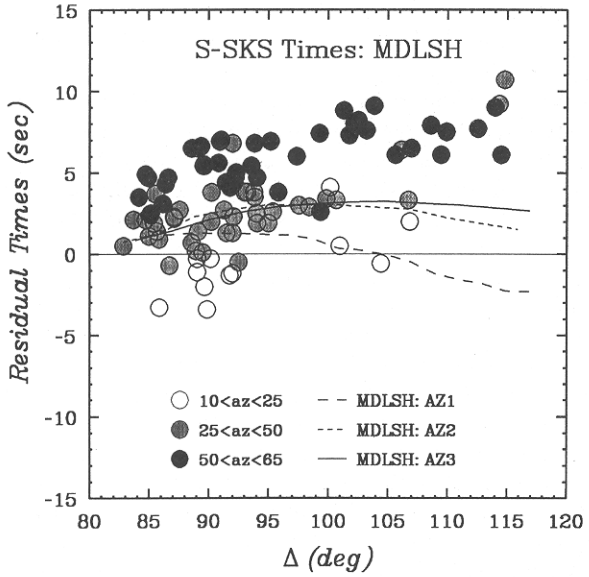

Fig. 11. Residual travel times (with respect to iasp91) of *S-SKS* (circles shaded to correspond to azimuth slice) are plotted as a function of distance along with the predictions from model MDLSH (lines) for the three cross sections AZ1, AZ2, and AZ3 shown in Figure 10.

AZ1, and poorly fits data from that azimuth (open circles). The line with short dashes is for AZ2 and fits the data for that azimuth (gray circles) within the scatter for distances <100° though is too small by several seconds at larger Δ (though data sampling are sparser for this azimuth at larger ranges.) The solid line is the prediction for AZ3 and is too small by 2–3 s, though the prediction has the approximate shape of the trend of the data. Also, the MDLSH predictions for AZ1, AZ2, and AZ3 are all nearly the same near 85°, where the data visibly group separately for the different azimuths. At distances larger than 105°, the MDLSH predictions have the relative trend of $\delta T_{S\text{-}SKS}(\mathrm{AZ3}) > \delta T_{S\text{-}SKS}(\mathrm{AZ2}) > \delta T_{S\text{-}SKS}(\mathrm{AZ1})$, which qualitatively agrees with the observations.

As an alternative attempt at modeling the observations with MDLSH, the residuals in the bottom four layers of the mantle (the bottom 1075 km of the lower mantle) were doubled in value to produce model "MDLSH+" (Figure 12). Such an exercise is arbitrary but may be justified due to an ambiguity in the choice of damping parameters used in originally constructing MDLSH (T. Tanimoto, personal communication, 1992). As Figure 12 shows, this emphasizes the growth of the lower mantle slow anomaly from Figure 12*a* to 12*c*. It also accentuates the fast lower mantle

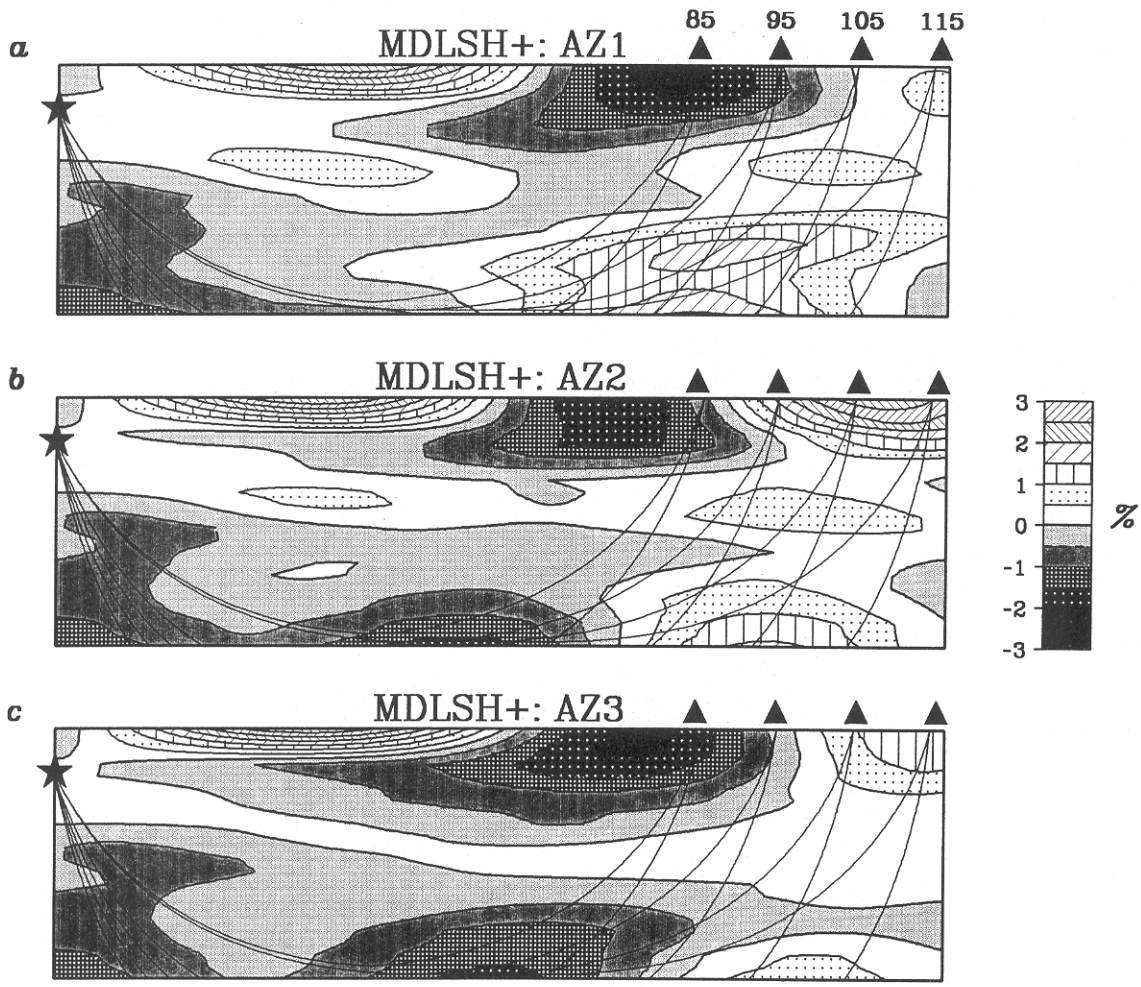

Fig. 12. Whole mantle cross sections from model MDLSH+, which is MDLSH of *Tanimoto* [1990] with residuals in bottom four layers doubled. Cross sections are for (*a*) AZ1, (*b*) AZ2, and (*c*) AZ3. V_S perturbations in percent are shown, where dark regions are slower than average, white and hatched regions are faster than average. See Figure 10 caption and text for more information.

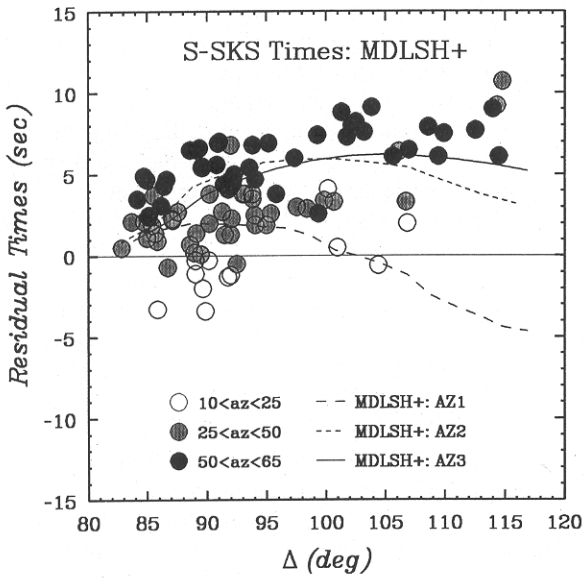

Fig. 13. Residual travel times (with respect to iasp91) of *S-SKS* (circles shaded to correspond to azimuth slice) are plotted as a function of distance along with the predictions from model MDLSH+ (lines) for the three cross sections AZ1, AZ2, and AZ3 shown in Figure 12.

anomaly underneath the receivers in Figure 12*a*. The $\delta T_{S\text{-}SKS}$ residuals predicted for MDLSH+ are compared to observations in Figure 13. All plotting conventions are the same as Figure 11. A first-order affect of doubling δV_S in the bottom four layers is to enlarge the positive $\delta T_{S\text{-}SKS}$ predictions and decrease the negative $\delta T_{S\text{-}SKS}$ predictions (from those in Figure 11). Doing this predicts *S-SKS* difference times for AZ1 and AZ2 that are incompatible with the data. However, the increased size of the mid-Pacific lower mantle slow anomaly in Figure 12*c* increases the predicted $\delta T_{S\text{-}SKS}$ for that cross section, and the fit to the data for that azimuth (solid circles) is greatly improved. Given the scatter in the data of $\approx\pm 2$ s for that azimuth, we consider this a good fit. In doubling the size of the δV_S residuals in the bottom four layers of the mantle, the resulting *S-SKS* travel time residuals are roughly doubled (compare Figures 11 and 13). This is expected since $\delta T_{S\text{-}SKS}$ times are very sensitive to the lowermost mantle.

In summarizing the predictions of MDLSH, the following may be stated: (1) $\delta T_{S\text{-}SKS}$ predictions for the most northerly azimuth cross-section AZ1 from Fiji-Tonga to North America differ from observations; (2) at distances <100°, $\delta T_{S\text{-}SKS}$ predictions for AZ2 are fair to good, and within the scatter of the data; (3) when δV_S in the bottom four layers (bottom 1075 km of mantle) of MDLSH is doubled, the $\delta T_{S\text{-}SKS}$ predictions for AZ3 are greatly improved, resulting in a fit for the whole distance range within the scatter of the data, though this causes predictions for AZ1 and AZ2 to increasingly differ from the observations. A combination of the two models MDLSH and MDLSH+ may in turn provide good fits to data from both of the azimuths AZ2 and AZ3; however, predictions from AZ1 disagree with our observations.

Model SH.10c.17 Predictions

Whole mantle cross sections for the shear wave velocity model SH.10c.17 of *Masters et al.* [1992] are presented in Figure 14 for the great circle paths in Figure 9 (again, Figures 14*a*, 14*b*, and 14*c* correspond to AZ1, AZ2, and AZ3, respectively).

A first-order difference between this model and MDLSH (or MDLSH+) is the location of the lower mantle slow anomaly: in SH.10c.17, the slow anomaly is roughly 2000 km closer to the source side of the ray paths (compare Figures 12*c* and 14*c*). Other features, such as upper mantle structure, also differ. The $\delta T_{S\text{-}SKS}$ predictions of SH.10c.17 are presented along with the observations in Figure 15. For this model, the $\delta T_{S\text{-}SKS}$ predictions for all three azimuths are within a ±3 s range with respect to iasp91. This is much smaller than the range of the data, where the anomalies are as large as 8–9 s. However, the SH.10c.17 predictions for AZ1 (line with long dashes) are within the scatter of the data for that azimuth (open circles) for the distance range of the observations. Also, the SH.10c.17 predictions for AZ2 (line with short dashes) provide a fit to the data for that azimuth (gray circles) within the scatter up to near 95°. For distances greater than 95°, SH.10c.17 underpredicts the observations. For AZ3 (solid line), the SH.10c.17 predictions of $\delta T_{S\text{-}SKS}$ are several seconds smaller than the observations. The reason that the $\delta T_{S\text{-}SKS}$ predictions for this azimuth are not larger than 1–2 s is due to the large lower mantle, slightly fast anomaly in Figure 14*c*. From Figure 14*a* to 14*c*, this anomaly becomes less fast, though in Figure 14*c* there is still a large enough negative contribution from this anomaly to counter the slow lower mantle anomaly on the source side of the path.

Summarizing the predictions of SH.10c.17: (1) $\delta T_{S\text{-}SKS}$ predictions for the most northerly azimuth cross section AZ1 from Fiji-Tonga to North America provide a fair fit to the data within the scatter; (2) at distances <95°; $\delta T_{S\text{-}SKS}$ predictions for AZ2 are fair to good and within the scatter of the data; (3) the $\delta T_{S\text{-}SKS}$ predictions for AZ3 are several seconds smaller than the average of the data for that azimuth; (4) for the entire distance range, predictions of $\delta T_{S\text{-}SKS}(\text{AZ3}) > \delta T_{S\text{-}SKS}(\text{AZ2}) > \delta T_{S\text{-}SKS}(\text{AZ1})$, which qualitatively agrees with the observations; and (5) there is not substantial "growth" of the low velocity D″ anomaly as seen in the other models.

Model SH12_WM13 Predictions

Whole mantle cross sections for the shear wave velocity model SH12_WM13 of *Su et al.* [1992] are presented in Figure 16 for the great circle paths AZ1, AZ2, and AZ3. For these cross sections, model SH12_WM13 is very similar to SH.10c.17 in Figure 14. The main difference is that the sizes of the SH12_WM13 anomalies are larger and there is a more pronounced increase in the low-velocity region toward AZ3. Of significance is the increased size of the lower mantle slow anomaly in Figure 16*c* on the source side of the path. This serves to further slow down *S* relative to *SKS*, which in principle will give a better fit to the observations. This slow anomaly, as in SH.10c.17, is ≈2000 km closer to the source side of the path than that of MDLSH (and MDLSH+, see Figures 16*c* and 12*c*). The $\delta T_{S\text{-}SKS}$ predictions of SH12_WM13 are compared to the data in Figure 17. The predictions for AZ1 (long dashes) are 1–2 s larger than observations (open circles) for distances <95°, though at larger distances they fit the mean of the remaining AZ1 data points. SH12_WM13 predictions for AZ2 (short dashes) are

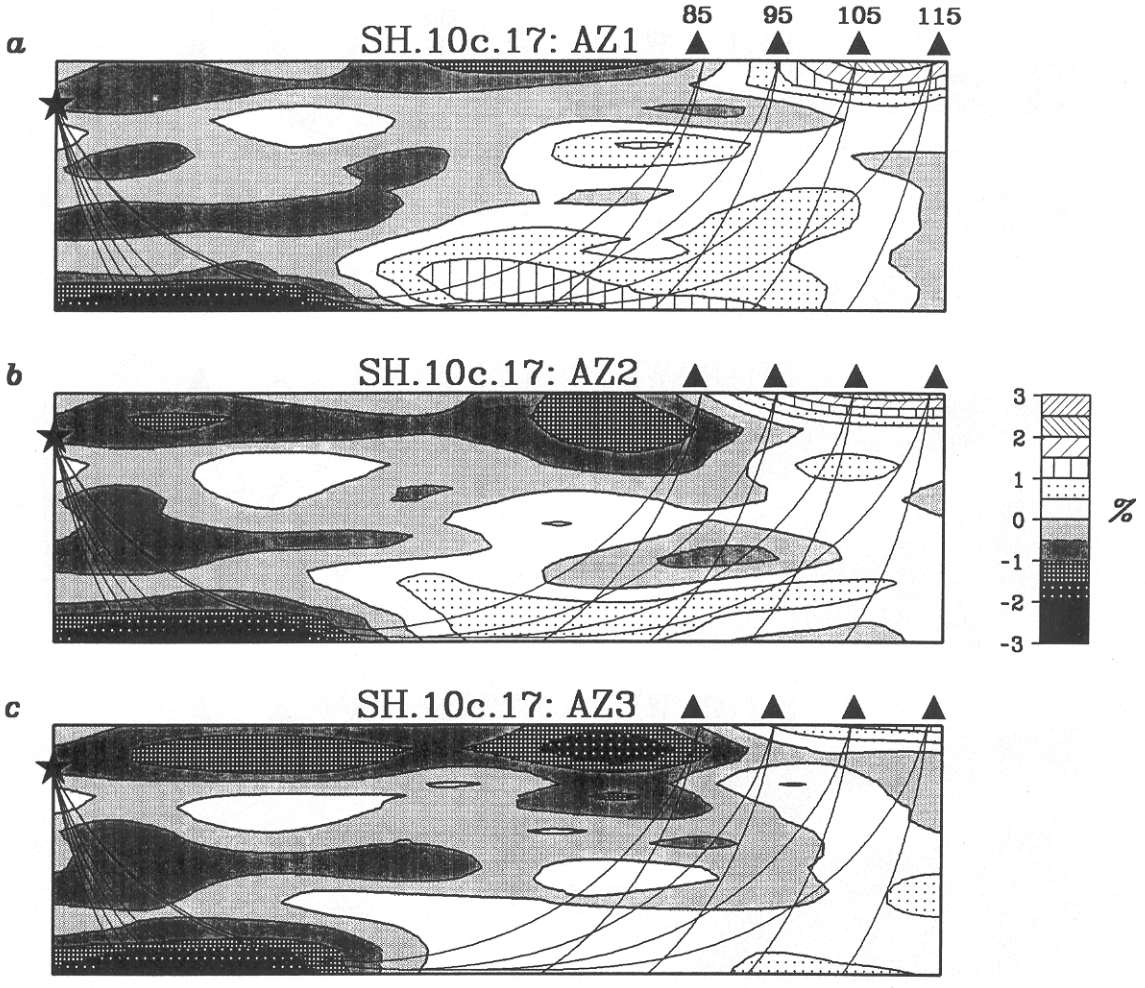

Fig. 14. Whole mantle cross sections from model SH.10c.17 of *Masters et al.* [1992] with cross sections for (*a*) AZ1, (*b*) AZ2, and (*c*) AZ3. V_S perturbations in percent are shown, where dark regions are slower than average, white and hatched regions are faster than average. See Figure 10 caption and text for more information.

within the scatter of the data (gray circles) for nearly the entire distance range (excluding only two anomalous points at 114°). For the azimuth AZ3, the predictions (solid line) are within the scatter of the observations (solid circles) for up to around 100°. For larger ranges, SH12_WM13 predicts $\delta T_{S\text{-}SKS}$ 2–3 s smaller than observations. The size of the relative differences in the SH12_WM13 predictions for the three different azimuths is very close to that of the observations.

For model SH12_WM13, we summarize as follows: (1) the first-order fit to the data for all three azimuths is fair to good within the scatter of the data, and more specifically: (2) $\delta T_{S\text{-}SKS}$ predictions for AZ1 provide a fair fit to the data within the scatter for distances >95°; (3) predictions for AZ2 are within the scatter of the data for the entire distance range (except for two data at 114°);(4) the $\delta T_{S\text{-}SKS}$ predictions for AZ3 are also with the scatter of the observations for distances <100°; and (5) the relative differences of the predictions for the three different azimuths roughly match relative differences of the observations from the different azimuth slices.

DISCUSSION

In comparing direct measurements of the observed differential travel times of S and SKS phases with those predicted

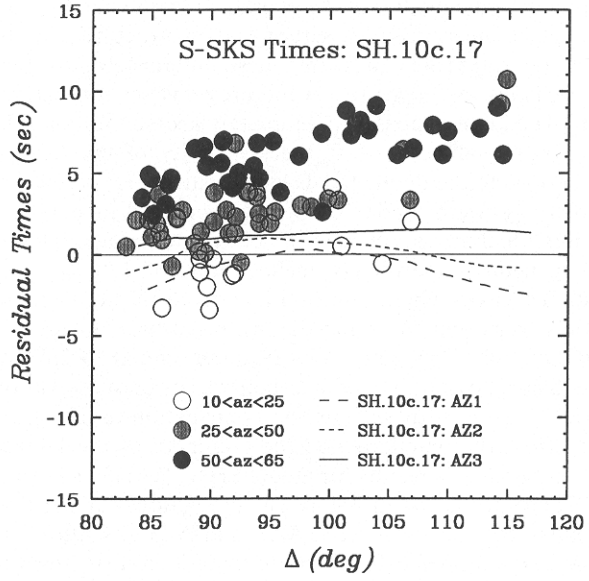

Fig. 15. Residual travel times (with respect to iasp91) of S-SKS (circles shaded to correspond to azimuth slice) are plotted as a function of distance along with the predictions from model SH.10c.17 (lines) for the three cross sections AZ1, AZ2, and AZ3 shown in Figure 14.

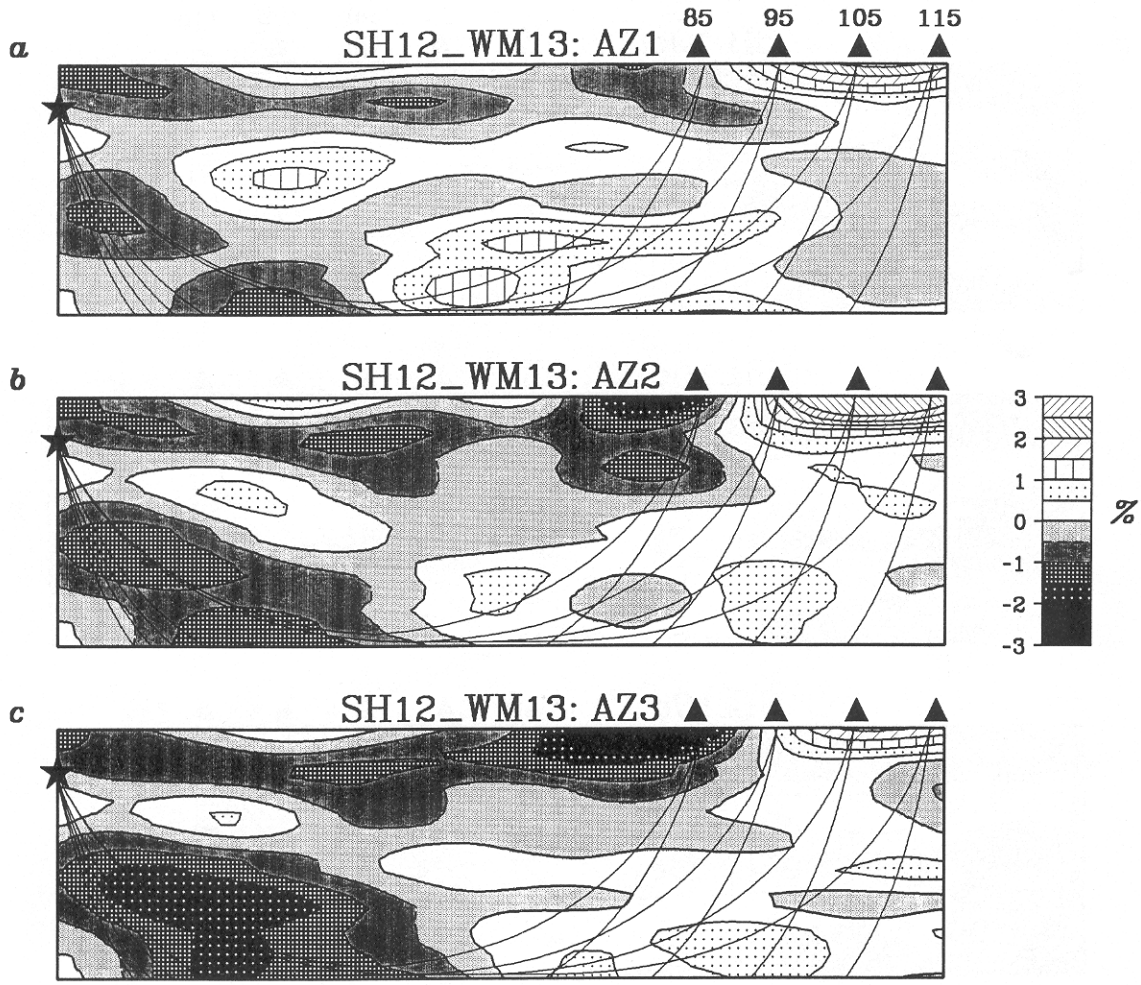

Fig. 16. Whole mantle cross sections from model SH12_WM13 of *Su et al.* [1992] with cross sections for (*a*) AZ1, (*b*) AZ2, and (*c*) AZ3. V_S perturbations in percent are shown, where dark regions are slower than average, white and hatched regions are faster than average. See Figure 10 caption and text for more information.

by tomographic models of the mantle, an understanding may be gained concerning what part of Earth's structure plays the most important role in affecting these difference times. Such comparisons, as presented in the previous section, suggest that 3-D mantle models may ultimately account for all of the $T_{S\text{-}SKS}$ anomalies. To test the sensitivity of the $\delta T_{S\text{-}SKS}$ predictions to the depth of 3-D mantle structure, predictions of $\delta T_{S\text{-}SKS}$ were made for the tomographic models with various thicknesses of the upper mantle made laterally homogeneous. Specifically, calculations of $\delta T_{S\text{-}SKS}$ were made for cases where contributions from the tomographic models were limited to the depth ranges 0–2891 km, 670–2891 km, 1022–2891 km, 1555–2891 km, and 1816–2891 km (which correspond to depths of boundaries between various model layers.) In these runs, no contribution to $\delta T_{S\text{-}SKS}$ is made from the mantle above the boundary of the 1-D and 3-D sections. The results for model SH12_WM13 of *Su et al.* [1992] are presented in Figure 18. Predictions for the three azimuth cross sections AZ1, AZ2, and AZ3 of Figure 9 are shown. The upper 670 km of the mantle contributes very little to the predicted *S-SKS* differential travel time. This is seen from the nearly complete overlap of the solid curves for the whole mantle, and the short-dashed curve for the 670–2891 km region. (Also, the predictions are made with the source at 500 km depth, so the uppermost mantle is tra-

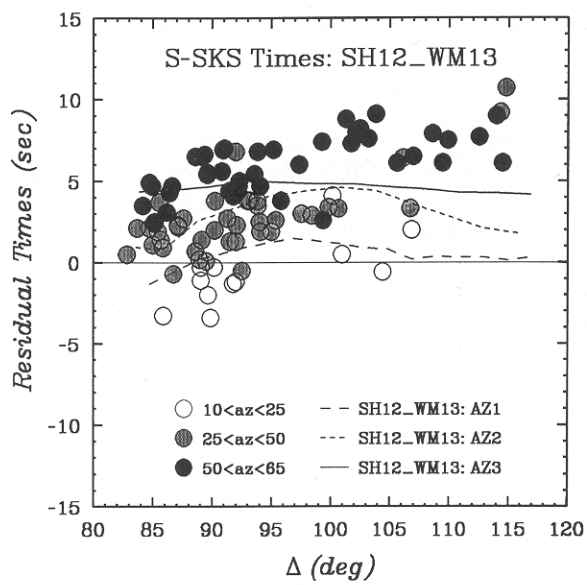

Fig. 17. Residual travel times (with respect to iasp91) of *S-SKS* (circles shaded to correspond to azimuth slice) are plotted as a function of distance along with the predictions from model SH12_WM13 (lines) for the three cross sections AZ1, AZ2, and AZ3 shown in Figure 16.

versed only on the receiver side of the paths.) In fact, ignoring the upper 1500 km or so of the mantle only produces deviations of less than one second from the whole mantle 3-D model predictions. Even with the 3-D mantle contributions limited to the bottom 1000 km of the mantle, the shapes of the curves for the different azimuths are basically the same, and the predictions are early on average by only ≈1 s. It makes intuitive sense that the anomalies in S-SKS times can be produced synthetically (for this region) solely from the bottom 1500 km of a 3-D mantle, with lateral homogeneity above 1500 km depth, because it is in the deeper portion of the mantle that the paths of S and SKS diverge the most. The upper mantle of the tomography models would affect the S-SKS times more if the lateral scale lengths of the anomalies were smaller. However, at present, with imaging of features with scale lengths of the order of 3000 km and greater, upper mantle affects on these predicted times are negligible. This is probably not the case in the real Earth, however. The difference in takeoff angle between S and SKS for a 500-km-deep source is around 10° at 85° in epicentral distance, and increases to about 15° at 115° in distance. For such takeoff angle differences, small scale-length heterogeneities surely play an important role. An example of such would be near-source slab diffraction as proposed by *Cormier* [1989], though using deep focus events may help to minimize such effects.

In making $\delta T_{S\text{-}SKS}$ predictions for the tomography models, the assumption was made that the ray paths are for a laterally homogeneous Earth structure. We are presently unable to assess the validity of this assumption, though the features of the tomographic models are much larger than the wavelengths of the seismic waves analyzed and presumably contribute negligibly to bending of the ray paths as to significantly affect the difference times. Also assumed was that the outer core does not vary laterally, and the outer core

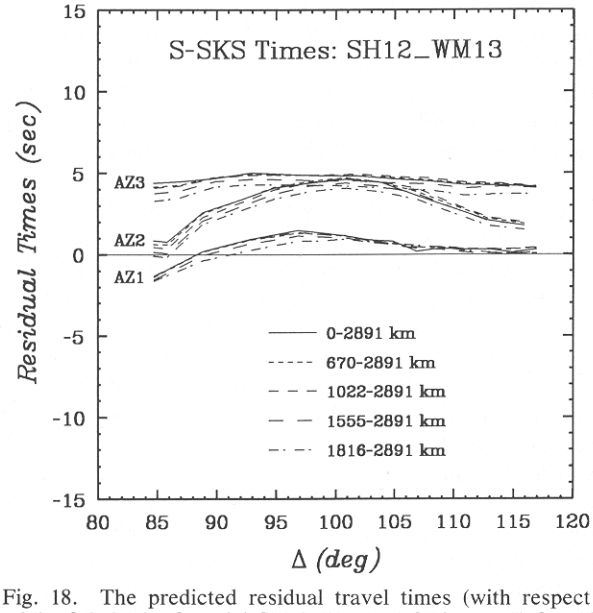

Fig. 18. The predicted residual travel times (with respect to iasp91) of S-SKS of model SH12_WM13 (of Figure 17) for AZ1, AZ2, and AZ3 (solid lines). Also plotted are predictions of residuals for various vertical thicknesses of 3-D cross sections of SH12_WM13 where mantle above these 3-D sections is laterally homogeneous (dashed lines). The depths above correspond to depth ranges of the 3-D sections.

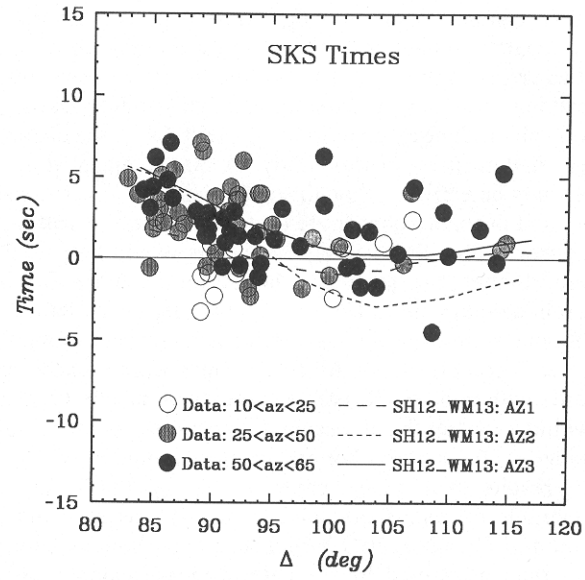

Fig. 19. Residual times of SKS (with respect to iasp91, circles shaded to correspond to azimuth slice) along with predictions of model SH12_WM13 [*Su et al.*, 1992] for AZ1, AZ2, and AZ3 cross sections of Figure 16 (lines).

from the iasp92 reference model was used [*Kennett and Engdahl*, 1991]. As mentioned earlier, the $\delta T_{S\text{-}SKS}$ time predictions of Figures 11, 13, 15, and 17 may be adjusted to accommodate the predictions of the other core models in Figure 8 by simply adding to the $\delta T_{S\text{-}SKS}$ prediction the subtraction (from Figure 8*b*): T_{SKS}(iasp91) − T_{SKS}(preferred core model). The T_{SKS} times alone cannot be used to determine outer core structure without subtracting out a mantle model first. Figure 19 shows the observed δT_{SKS} times of Figures 6*b*, along with predictions for δT_{SKS}, where SKS has traversed the whole mantle model SH12_WM13 of *Su et al.* [1992]. Of particular significance is the δT_{SKS} prediction for AZ3 (the cross section in Figure 16*c*). The source-side lower mantle anomaly significantly slows down SKS at smaller distances, as Figure 19 displays. However, the scatter in the absolute travel times is easily observed as addressed earlier in Figure 2 and not explained by present global tomographic models which must be smoothed for stability. Thus we have chosen to concentrate on the differential times of S and SKS with respect to the 3-D models instead of either phase individually because of the reduction in scatter seen in Figure 6 in going from δT_S and δT_{SKS} times to the $\delta T_{S\text{-}SKS}$ times. Though it is important to note from the different curves in the Figure 19 how 3-D mantle structure can strongly affect the SKS times.

Two other possible structural features that may affect S-SKS difference times are CMB topography and anisotropy. A CMB undulation of ±5 km at the entering and exiting points for SKS would only change the SKS time, and hence $T_{S\text{-}SKS}$, by about ±0.2 s. This is a negligible contribution given the size of the S-SKS anomalies. In examining S and S_{diff} on the radial and tangential components of the rotated seismograms (at distances where SV_{diff} is still observable), shear wave splitting was not apparent; hence this affect is assumed not to play a role in the $T_{S\text{-}SKS}$ times. Nevertheless, using the azimuth binning of Figure 5 still results in scatter of the order of seconds, as seen in Figure

6c. This can be a result of deep mantle structure varying on scale lengths smaller than the azimuth binning chosen, as well as errors in the $T_{S\text{-}SKS}$ times due to source mislocation or picking errors. A mislocation in a 500-km-deep event by 50 km will produce an error in $T_{S\text{-}SKS}$ of 0.7 s for the distance range of data used in this study. A 50-km mislocation in depth may be extreme, though smaller mislocation errors are likely and probably contribute up to ±0.5 s to the scatter in our observations. Relocating the events would help in this regard, though the scatter is larger than ±0.5 s for the different azimuth slices (Figure 7) and must be attributed to additional sources, such as strong near-source anomalies (e.g., slab complexities). All travel times were picked from records with good SNR, and accuracy can usually be made to within a few tenths of a second, depending on the record. Placing a ±0.5-s error bound on measurements of T_S or T_{SKS} results in a ±1.0-s error for $T_{S\text{-}SKS}$ times. This is comparable to results obtained from $T_{SS\text{-}S}$ as reported by *Grand and Helmberger* [1985]. These error bounds may be larger than warranted by the careful measurements. However, since we make no effort at a more rigorous error analysis, this ± bound is chosen for discussion purposes. If all of the above errors were to constructively add, e.g., 0.2 s (5 km CMB topography) + 0.7 s (50 km depth mislocation) + 1.0 s (picking error), a ≈ 2 s error would result. This is of the order of the scatter seen in Figure 7, though it is unlikely that all of the scatter is due to such extremes. It is very likely that the scatter is also due to smaller scale heterogeneities than the scale length of the azimuth slices of Figure 5. For the same source-receiver geometry, *Schweitzer* [1988] concluded that tomography models are too smooth to explain anomalies seen in the *SKS-SKKS* data set. Realistically, the $\delta T_{S\text{-}SKS}$ times do not smoothly change from the smallest to largest azimuth for the source-receiver geometry of this data set. Rather, the azimuth binning was chosen as to represent the dominant trend in the data, which is readily seen in Figure 7. Unexplained scatter about the general trends of Figure 7 may be an indication of small-scale deep Earth anomalies of a few tens of kilometers encountered by *S* and *SKS*. Such anomalies are presently assumed to be the cause of precursors to the PKP caustic [*Haddon and Cleary*, 1974]. Further studies on scattering phenomena associated with particularly anomalous regions and their affect on diffracted *P* and *S* waves may help resolve such issues. Errors in estimation of the hypocentral locations may also be an important contributor to the scatter.

All three models tested in this study have lower mantle velocities beneath the central Pacific that are slower than average (Figure 9). The *S-SKS* observations are also best explained by an anomalously slow lower mantle beneath the mid-Pacific. These slower velocities may indicate a hotter than average lower mantle. The lowermost mantle surrounding the Pacific contains faster than average velocities in the models of Figure 9, which may indicate colder than average regions. These patterns may be related to large-scale convection in the lower mantle beneath the Pacific: the surrounding cold regions representing downward mantle flow; the central hot region relating to mantle upwelling, possibly relating to a plume source.

The details of the D″ anomalies of the different models in Figure 9 differ. *S-SKS* times may be used as an added constraint in future tomographic inversions to help resolve such differences. These times provide a powerful constraint between the deep mantle regions of *SKS* entrance and exit points into the core, and the deep mantle region traversed by *S* (or S_{diff}) near the midpoint of the source-receiver ray path. Abundant *S-SKS* data are available for such a study due to the frequent and numerous circum-Pacific events. Such results may be used to subtract off mantle contributions to *SKS-SKKS* times in effort to address the question of core-side heterogeneity (as from *Kohler and Tanimoto* [1992]).

CONCLUSIONS

The travel times of *S* and *SKS* from long-and short-period recordings of deep-focus Fiji-Tonga events recorded in North America by CSN and WWSSN stations exhibit a strong azimuthal dependence. The differential time $T_{S\text{-}SKS}$ proves to be an effective measure of lower mantle structure. Azimuths to the north from the source region are generally accompanied by small to average $\delta T_{S\text{-}SKS}$ times, suggesting on average a normal lower mantle structure; while $\delta T_{S\text{-}SKS}$ times from azimuths trending toward the northeast are anomalously large (by up to 9 s), implying a slower than average lower mantle beneath the central Pacific. This finding is also seen in tomography models of the region. $T_{S\text{-}SKS}$ time predictions from the three different tomography models studied illustrate how a large lower mantle V_S anomaly of around −2% or more (slow V_S) can produce $T_{S\text{-}SKS}$ anomalies of the size of the observations from the slow azimuth AZ3. However, anomalies of scale lengths smaller than those in the tomographic models may be responsible for some of the inconsistencies in the predictions of the 3-D models when compared to observations.

Predictions of SH12_WM13 [*Su et al.*, 1992] provide a reasonable overall fit to the observations, though the most northerly azimuth AZ1 observations suggest a slightly faster path than that predicted, and observations at the largest distances for AZ3 suggest a slightly slower path than predicted (Figure 17). Model SH.10c.17 [*Masters et al.*, 1992] underpredicts the size of the $\delta T_{S\text{-}SKS}$ anomalies to the slowest azimuth AZ3 (Figure 15), though provides a reasonable prediction for the faster northerly azimuth AZ1, due to a large lower mantle fast anomaly on the receiver side of the structure (Figure 14*a*). Predictions from model MDLSH [*Tanimoto*, 1990] with residuals in the bottom four layers doubled (model MDLSH+) provide a good fit to the data for the AZ3 path (Figure 13), though the other two paths AZ1 and AZ2 differ from observations. The slow anomaly in MDLSH+ responsible for producing large $\delta T_{S\text{-}SKS}$ predictions for AZ3 is about 2000 km to the northeast from the location of the slow feature in SH12_WM13 (as well as in SH.10c.17) responsible for the same effect. This suggests a problem of nonuniqueness in the finer details of deep Earth modeling from the phases *S* and *SKS* alone. However, the strong azimuthal dependence of the difference times for this region may provide a powerful constraint for 3-D lower mantle modeling. Finally, the use of a laterally varying outer core is not necessary to explain the anomalies of this data set, though such a scenario cannot be resolved with this data.

Acknowledgments. Special thanks to Toshiro Tanimoto, Guy Masters, and Wei-jia Su for providing their models and the necessary subroutines to read their models and to Steve Grand for

providing the program to predict travel times through 3-D models. Thanks also to Thorne Lay for reviewing the manuscript and for useful discussions concerning this work. Adam Dziewonski and Justin Revenaugh also provided useful reviews that helped to improved the manuscript. This research was supported by the National Science Foundation grant EAR-91-17781. Division of Geological and Planetary Sciences, California Institute of Technology contribution 5261.

REFERENCES

Cormier, V. F., Slab diffraction of *S* waves, *J. Geophys. Res.*, *94*, 3006–3024, 1989.

Dziewonski, A. M., and D. L. Anderson, Preliminary reference Earth model (PREM), *Phys. Earth Planet. Inter.*, *25*, 297–356, 1981.

Dziewonski, A., and F. Gilbert, The effect of small, aspherical perturbations on travel times and a re-examination of the corrections for ellipticity, *Geophys. J. R. Astron. Soc.*, *44*, 7–17, 1976.

Dziewonski, A., and J. H. Woodhouse, Global images of the Earth's interior, *Science*, *236*, 37–48, 1987.

Garnero, E. J., D. V. Helmberger, and G. Engen, Lateral variations near the core-mantle boundary, *Geophys. Res. Lett.*, *15*, 609–612, 1988.

Grand, S. P., Tomographic inversion for shear velocity beneath the North American, *Geophys. J. R. Astron. Soc.*, *76*, 399–438, 1987.

Grand, S. P., and D. V. Helmberger, Uppermantle shear structure beneath Asia from multi-bounce *S* waves, *Phys. Earth Planet. Inter.*, *41*, 154–169, 1985.

Graves, R. W., and D. V. Helmberger, Upper mantle cross section from Tonga to Newfoundland, *J. Geophys. Res.*, *93*, 4701–4711, 1988.

Haddon, R. A. W., and J. R. Cleary, Evidence for scattering of seismic *PKP* waves near the mantle-core boundary, *Phys. Earth Planet. Inter.*, *8*, 211–234, 1974.

Hales, A. L., and J. L. Roberts, The velocities in the outer core, *Bull. Seismol. Soc. Am.*, *61*, 1051–1059, 1971.

Kennett, B. L. N., and E. R. Engdahl, Traveltimes for global earthquake location and phase identification, *Geophys. J. Int.*, *105*, 429–465, 1991.

Kind, R., and G. Müller, The structure of the outer core from *SKS* amplitudes and travel times, *Bull. Seismol. Soc. Am.*, *67*, 1541–1554, 1977.

Kohler, M. D., and T. Tanimoto, One-layer global inversion for the outermost core velocity, *Phys. Earth Planet. Inter.*, *72*, 173–184, 1992.

Lay, T., and D. V. Helmberger, Body-wave amplitude and travel-time corrections across North America, *Bull. Seismol. Soc. Am.*, *73*, 1063–1076, 1983.

Lay, T., and C. J. Young, The stably-stratified outermost core revisited, *Geophys. Res. Lett.*, *17*, 2001–2004, 1990.

Li, X., D. Giardini, and J. H. Woodhouse, Large-scale three-dimensional even-degree structure of the Earth from splitting of long-period normal modes, *J. Geophys. Res.*, *96*, 551–577, 1991.

Masters, G., H. Bolton, and P. Shearer, Large-scale 3-dimensional structure of the mantle (abstract), *Eos Trans. AGU*, *73*, 201, 1992.

Randall, M. J., *SKS* and seismic velocities in the outer core, *Geophys. J. R. Astron. Soc.*, *21*, 441–445, 1970.

Schweitzer, J., Laufzeiten und amplituden der phasen SKS und SKKS und die struktur des äusseren erdkerns, Ph.D. thesis, 117 pp., Inst. für Meteorol. und Geophys. der Johann Wolfgang Goethe-Univ., Frankfurt, Germany, 1984.

Schweitzer, J., Anomalous *S*-phases and the structure in the lower mantle and at the core mantle boundary beneath the central Pacific, *Terra Cognita*, *8*, 152, 1988.

Schweitzer, J., and G. Müller, Anomalous difference traveltimes and amplitude ratios of *SKS* and *SKKS* from Tonga-Fiji events, *Geophys. Res. Lett.*, *13*, 1529–1532, 1986.

Sipkin, S. A., and T. H. Jordan, Multiple *ScS* travel times in the western Pacific: Implications for mantle heterogeneity, *J. Geophys. Res.*, *85*, 853–861, 1980.

Souriau, A., and G. Poupinet, A study of the outermost liquid core using differential travel times of the *SKS*, *SKKS*, and *S3KS* phases, *Phys. Earth Planet. Inter.*, *68*, 183–199, 1991.

Stevenson, D. J., Limits on lateral density and velocity variations in the Earth's outer core, *Geophys. J. R. Astron. Soc.*, *88*, 311–319, 1987.

Su, W., R. L. Woodward, and A. M. Dziewonski, Joint inversions of travel-time and waveform data for the 3-D models of the Earth up to degree 12 (abstract), *Eos Trans. AGU*, *73*, 201–202, 1992.

Tanimoto, T., Long-wavelength *S*-wave velocity structure throughout the mantle, *Geophys. J. Int.*, *100*, 327–336, 1990.

Woodward, R. L., and G. Masters, Lower-mantle structure from *ScS-S* differential travel times, *Nature*, *352*, 231–233, 1991.

E. J. Garnero and D. V. Helmberger, Seismological Laboratory 252-21, California Institute of Technology, Pasadena, CA 91125.

(Received August 5, 1992;
revised December 30, 1992;
accepted January 15, 1993.)